



UvA-DARE (Digital Academic Repository)

The Featureless HST/WFC3 Transmission Spectrum of the Rocky Exoplanet GJ 1132b

No Evidence for a Cloud-free Primordial Atmosphere and Constraints on Starspot Contamination

Libby-Roberts, J.E.; Berta-Thompson, Z.K.; Diamond-Lowe, H.; Gully-Santiago, M.A.; Irwin, J.M.; Kempton, E.M.-R.; Rackham, B.V.; Charbonneau, D.; Désert, J.-M.; Dittman, J.A.; Hofmann, R.; Morley, C.V.; Newton, E.R.

DOI

[10.3847/1538-3881/ac75de](https://doi.org/10.3847/1538-3881/ac75de)

Publication date

2022

Document Version

Final published version

Published in

Astronomical Journal

License

CC BY

[Link to publication](#)

Citation for published version (APA):

Libby-Roberts, J. E., Berta-Thompson, Z. K., Diamond-Lowe, H., Gully-Santiago, M. A., Irwin, J. M., Kempton, E.M.-R., Rackham, B. V., Charbonneau, D., Désert, J.-M., Dittman, J. A., Hofmann, R., Morley, C. V., & Newton, E. R. (2022). The Featureless HST/WFC3 Transmission Spectrum of the Rocky Exoplanet GJ 1132b: No Evidence for a Cloud-free Primordial Atmosphere and Constraints on Starspot Contamination. *Astronomical Journal*, 164(2), [164]. <https://doi.org/10.3847/1538-3881/ac75de>

General rights

It is not permitted to download or to forward/distribute the text or part of it without the consent of the author(s) and/or copyright holder(s), other than for strictly personal, individual use, unless the work is under an open content license (like Creative Commons).

Disclaimer/Complaints regulations

If you believe that digital publication of certain material infringes any of your rights or (privacy) interests, please let the Library know, stating your reasons. In case of a legitimate complaint, the Library will make the material inaccessible and/or remove it from the website. Please Ask the Library: <https://uba.uva.nl/en/contact>, or a letter to: Library of the University of Amsterdam, Secretariat, Singel 425, 1012 CP Amsterdam, The Netherlands. You will be contacted as soon as possible.



The Featureless HST/WFC3 Transmission Spectrum of the Rocky Exoplanet GJ 1132b: No Evidence for a Cloud-free Primordial Atmosphere and Constraints on Starspot Contamination

Jessica E. Libby-Roberts^{1,2}, Zachory K. Berta-Thompson¹, Hannah Diamond-Lowe³, Michael A. Gully-Santiago⁴, Jonathan M. Irwin⁵, Eliza M.-R. Kempton⁶, Benjamin V. Rackham^{7,12}, David Charbonneau⁵, Jean-Michel Désert⁸, Jason A. Dittmann⁹, Ryan Hofmann^{1,10}, Caroline V. Morley⁴, and Elisabeth R. Newton¹¹

¹Department of Astrophysical and Planetary Sciences, University of Colorado, Boulder, CO 80309, USA; jer5346@psu.edu

²Center for Exoplanets and Habitable Worlds, Pennsylvania State University, State College, PA, 16803, USA

³National Space Institute, Technical University of Denmark, Elektrovej 328, DK-2800 Kgs. Lyngby, Denmark

⁴The University of Texas at Austin Department of Astronomy, 2515 Speedway, Stop C1400, Austin, TX 78712, USA

⁵Center for Astrophysics, Harvard and Smithsonian, 60 Garden Street, Cambridge, MA, 02138, USA

⁶Department of Astronomy, University of Maryland, College Park, MD 20742, USA

⁷Department of Earth, Atmospheric and Planetary Sciences, and Kavli Institute for Astrophysics and Space Research, Massachusetts Institute of Technology, Cambridge, MA 02139, USA

⁸Anton Pannekoek Institute for Astronomy, University of Amsterdam, 1090 GE Amsterdam, The Netherlands

⁹Max Planck Institute for Astronomy, Königstuhl 17, D-69117, Heidelberg, Germany

¹⁰National Solar Observatory, Boulder, CO 80309, USA

¹¹Department of Physics and Astronomy, Dartmouth College, Hanover, NH 03755, USA

Received 2021 May 19; revised 2022 April 20; accepted 2022 May 19; published 2022 July 19

Abstract

Orbiting an M dwarf 12 pc away, the transiting exoplanet GJ 1132b is a prime target for transmission spectroscopy. With a mass of $1.7 M_{\oplus}$ and radius of $1.1 R_{\oplus}$, GJ 1132b's bulk density indicates that this planet is rocky. Yet with an equilibrium temperature of 580 K, GJ 1132b may still retain some semblance of an atmosphere. Understanding whether this atmosphere exists and its composition will be vital for understanding how the atmospheres of terrestrial planets orbiting M dwarfs evolve. We observe five transits of GJ 1132b with the Wide Field Camera 3 (WFC3) on the Hubble Space Telescope (HST). We find a featureless transmission spectrum from 1.1 to $1.7 \mu\text{m}$, ruling out cloud-free atmospheres with metallicities $<300\times$ solar with $>4.8\sigma$ confidence. We combine our WFC3 results with transit depths from TESS and archival broadband and spectroscopic observations to find a featureless spectrum across 0.7 to $4.5 \mu\text{m}$. GJ 1132b therefore has a high mean molecular weight atmosphere, possesses a high-altitude aerosol layer, or has effectively no atmosphere. Higher-precision observations are required in order to differentiate between these possibilities. We explore the impact of hot and cold starspots on the observed transmission spectrum GJ 1132b, quantifying the amplitude of spot-induced transit depth features. Using a simple Poisson model, we estimate spot temperature contrasts, spot covering fractions, and spot sizes for GJ 1132. These limits, as well as the modeling framework, may be useful for future observations of GJ 1132b or other planets transiting similarly inactive M dwarfs.

Unified Astronomy Thesaurus concepts: Exoplanet atmospheres (487); Exoplanet atmospheric composition (2021); Extrasolar rocky planets (511); Exoplanets (498); Transmission spectroscopy (2133); Starspots (1572)

Supporting material: machine-readable table

1. Introduction

If our solar system's terrestrial planets and moons are any indicator, rocky exoplanets likely possess a diverse population of atmospheres. From the thick CO_2 -dominated atmosphere of Venus, out to the tenuous N_2 atmosphere of Pluto, the rocky worlds of our solar system have undergone significant atmospheric evolution (for a review, see Encrenaz & Coustenis 2018). Many terrestrial exoplanets likely experienced similar transformations, leading to a variety of atmospheres (e.g., Segura et al. 2003; Grenfell et al. 2007; Hu et al. 2012; Forget & Leconte 2014; Luger & Barnes 2015; Schaefer et al. 2016; Grenfell et al. 2020;

Kite & Barnett 2020). It is also possible that some rocky exoplanets never lost their primary atmospheres. Instead, they continue to maintain a slight H/He envelope consisting of $<1\%$ of their overall masses accreted from the planetary nebula (Owen et al. 2020). Characterizing these terrestrial atmospheres will be crucial for understanding the formation, evolution, and potential habitability of these rocky worlds.

Of interest for atmospheric characterization are the rocky planets orbiting nearby bright M dwarfs. The smaller stellar radii of these stars translates directly into larger transit depths for Earth-sized planets passing in front of them (Nutzman & Charbonneau 2008; Winn 2010). Moreover, these systems tend to be compact, with the habitable zone generally within 0.2 au of the star (Kopparapu et al. 2013). As the transit probability is inversely proportional to the semimajor axis, there is a higher likelihood of an M-dwarf planet transiting than one orbiting an FGK dwarf. Therefore, most super-Earth and Earth-sized planets amenable for transmission spectroscopy orbit nearby

¹² 51 Pegasi b Fellow

bright M dwarfs (e.g., Berta-Thompson et al. 2015; Gillon et al. 2016; Dittmann et al. 2017; Kostov et al. 2019; Vanderspek et al. 2019; Ment et al. 2019; Winters et al. 2019; Luque et al. 2019; Ment et al. 2021; Trifonov et al. 2021).

One notable planet for atmospheric study is the Earth-sized rocky planet, GJ 1132b. Discovered with the M_{Earth} survey (Berta-Thompson et al. 2015), this $1.130 \pm 0.056 R_{\oplus}$ and $1.66 \pm 0.23 M_{\oplus}$ rocky planet orbits a nearby inactive M3.5 dwarf (Hawley et al. 1996; Dittmann et al. 2017; Bonfils et al. 2018). GJ 1132b receives $19\times$ more bolometric insolation than Earth, implying a global equilibrium temperature of about 580 K (assuming uniform heat redistribution and Bond albedo of 0) making it far too hot to be habitable. GJ 1132b receives more stellar flux than Mercury, but its higher mass and surface gravity lead to the questions: Does GJ 1132b possess an atmosphere? And if so, what is its atmospheric composition?

GJ 1132b was targeted by ground-based observations seeking answers to these questions (Southworth et al. 2017; Diamond-Lowe et al. 2018). In broadband transit depths, Southworth et al. (2017) marginally detected hints of a low-metallicity atmosphere. This evidence was based primarily on a single anomalously deep z-band transit and required a 20% larger stellar radius than previously inferred. In contrast, Diamond-Lowe et al. (2018) observed a featureless spectrum between 700 and 1040 nm with an average precision of 100 ppm per wavelength bin (equivalent to 1.8 scale heights assuming a H/He mean molecular weight). Based on their higher-precision results, they disfavor a cloud-free atmosphere of $< 10\times$ solar metallicity by volume. This suggests either a secondary atmosphere with a higher mean molecular weight, high-altitude aerosols, or no atmosphere around GJ 1132b. The broadband $4.5\ \mu\text{m}$ Spitzer channel and the M_{Earth} optical $0.7\text{--}1.0\ \mu\text{m}$ observations from Dittmann et al. (2017) do not by themselves strongly constrain possible atmospheres. They do provide a light-curve-derived stellar density that confirms a stellar radius in agreement with Diamond-Lowe et al. (2018) and Berta-Thompson et al. (2015).

Waalkes et al. (2019) searched for a deep Ly α ultraviolet transit of GJ 1132b using HST/STIS. They detected no transits but placed a 2σ upper limit of an exosphere at $7.3\times$ the optical planetary radius. From this, they argue that it is unlikely that GJ 1132b possesses an extended hydrogen envelope created from a leftover primary atmosphere or from the photodissociation of water. Based on the planet’s total high-energy irradiation estimated from the stellar Ly α emission, Waalkes et al. (2019) calculated a mass-loss upper limit of neutral hydrogen to be $0.86 \times 10^9\ \text{g s}^{-1}$, or one Earth ocean every 6 Myr.

Theoretical work shows that any atmosphere of a planet like GJ 1132b has been influenced by the intense X-ray and ultraviolet radiation and activity common to M dwarfs (France et al. 2016). M dwarfs exhibit more XUV flux relative to bolometric than G dwarfs, making M dwarfs more efficient drivers of atmospheric escape (Lopez & Fortney 2013; Owen & Wu 2017). Analysis of UV observations of a similar planet host, LHS 3844, back these theoretical arguments while supporting the hypothesis that any atmosphere surrounding GJ 1132b is secondary in nature (Diamond-Lowe et al. 2021).

Schaefer et al. (2016) modeled the evolution of GJ 1132b’s atmosphere in order to predict potential atmospheric compositions, tracking both atmospheric escape and mantle outgassing. They find that GJ 1132b would have required at least 5% of its initial mass to be water in order to retain a water-dominated

atmosphere today. As this would be unlikely for a planet forming interior to the snow line, Schaefer et al. (2016) argue that the most likely outcome is a tenuous atmosphere dominated by O₂ created by the photodissociation of H₂O. However, most of the hydrogen and some of the oxygen atoms produced from this process are lost to space through hydrodynamic drag or absorption into a magma ocean. Schaefer et al. (2016) briefly comment on a CO₂-dominated atmosphere, noting that adding significant CO₂ will prolong a surface magma ocean and enhance atmospheric loss. However, future exploration and modeling are required in order to test this hypothesis.

Here we investigate the existence of an atmosphere around GJ 1132b by observing its transmission spectrum from the Hubble Space Telescope (HST) Wide-Field Camera 3 (WFC3) between 1.1 and 1.7 μm . These observations enable a sensitive search for water-vapor absorption, provide observational constraints on possible atmospheric compositions, and test whether or not GJ 1132b was able to retain a primordial hydrogen-rich atmosphere.

However, stellar activity, especially unocculted stellar spots and faculae, have the potential to either mimic or mask planetary water features in the WFC3 bandpass (Rackham et al. 2018; Zhang et al. 2018). GJ 1132, with a rotation period of 130 days, is not young (Newton et al. 2018) but does show variability due to rotating starspots. Dittmann et al. (2017) attributed an offset between the M_{Earth} optical and Spitzer infrared transit depths to unocculted stellar spots. We therefore use available data to quantify the impact of GJ 1132’s stellar activity on the interpretation of planetary transmission spectra. As both GJ 1132b’s transmission and emission spectra are scheduled to be observed in Cycle 1 by the James Webb Space Telescope (JWST), quantifying the starspot contamination is crucial.

We present this work in the following sections. We outline the observations in Section 2 and detail the analysis of the broadband and spectroscopic light curves in Section 3. We present an analysis of the TESS light curve of GJ 1132 in this section as well, providing additional constraints on the system properties and ruling out the transit of GJ 1132c. Section 4 discusses the transmission spectrum and the possible atmospheric compositions for GJ 1132b. We quantify stellar contamination in the transmission spectrum in Section 5 before concluding in Section 6.

2. Observations and Data Reduction

2.1. Data

We observed five transits of GJ 1132b with WFC3/IR grism spectroscopy (GO #14758, PI Berta-Thompson). We used the G141 grism, providing stellar spectra at a resolution of $R = \lambda/\Delta\lambda = 130$ covering approximately 1.1–1.7 μm . Each visit consisted of one orbit used to settle WFC3’s optical and detector systematics (this orbit was discarded from analysis), one orbit before transit, one orbit in transit, and one orbit after transit. Phase constraints were set to maximize time in transit between Earth occultations, and the five scheduled visits together provided complete phase coverage of the transit, including both ingress and egress.

We gathered data with the 256×256 subarray, using the SAMP-SEQ = SPARS10 and NSAMP = 15 settings for a total photon-counting exposure time of 103s per exposure. To

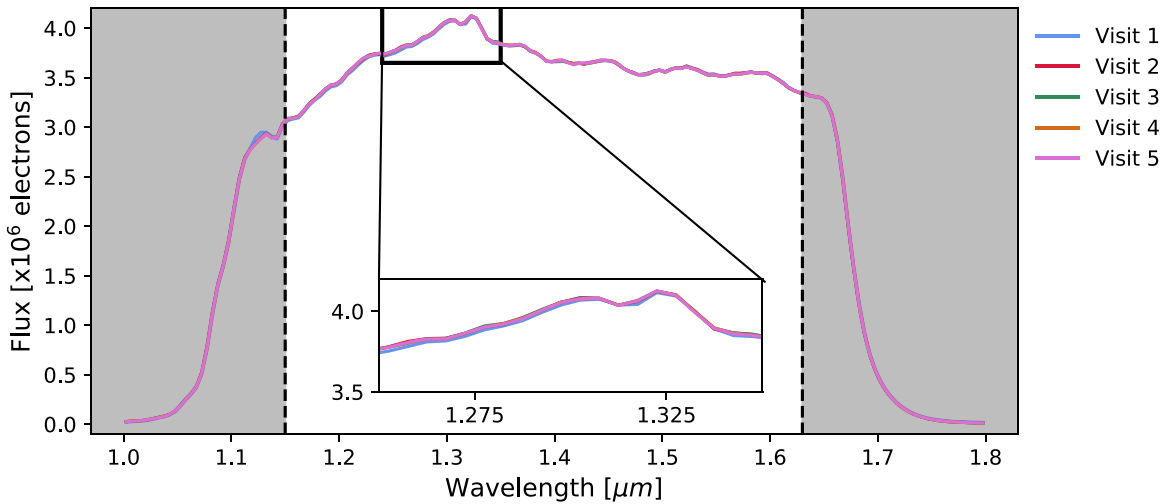


Figure 1. A comparison of the average stellar spectrum extracted for each visit. We find no evidence of significant contamination by other sources, as there is very little deviation in flux levels of the star across the five visits. The $1.15 \mu\text{m}$ and $1.63 \mu\text{m}$ are marked with dashed lines for comparison with Figure 2.

minimize the overheads associated with detector readout and/or memory buffer dumps, we used a round-trip spatial scan in the cross-dispersion direction. A scan rate of $0.2''$ per second kept the maximum fluence recorded on the detector at a safe level of about $24,000 \text{ e}^-/\text{pixel}$. For each exposure, 72s were lost to readout and scan resets, resulting in an overall photon-counting duty cycle of 58% for the 22 exposures gathered each orbit between Earth occultations.

GJ 1132 is near the Galactic plane ($b = 8^\circ$) and therefore in a crowded field. This presented a challenge for slitless spectroscopy due to the potential for multiple stars’ spectra to overlap. In planning the observations, we picked a combination of ORIENT constraints and scan rate to prevent overlap of any significant background stars with GJ 1132’s first-order spectrum during a single nondestructive read (see Section 2.2).

2.2. Reduction

We reduced each of the five WFC3 visits using the publicly available *iraclis* pipeline.¹³ We include a summary of the pipeline’s steps here; Tsiaras et al. (2016a, 2016b) provide a full description of the pipeline’s methodology. Starting with the raw, uncalibrated, spatially scanned spectroscopic images, *iraclis* performs the following: a zero-read subtraction, nonlinearity correction, dark correction, gain conversion, flat fielding, sky background subtraction, and bad-pixel and cosmic ray interpolation. To reduce nearby stellar contamination, *iraclis* performs a masking technique similar to that of Deming et al. (2013) by subtracting each read from the next (as opposed to the last read minus the first). *iraclis* calculates potential horizontal and vertical shifts in the scanned spectrum over time and determines the scan length for each image by approximating a Gaussian along the summed rows. Based off the direct image of GJ 1132, wavelengths are assigned and the wavelength-dependent flat field is applied. *iraclis* reports times in units of HJD, which we converted to BJD_{TDB} using the time utilities code of Eastman et al. (2010).¹⁴

We extracted the 1D spectrum by applying a 166-pixel-wide aperture along the dispersion axis and summing along the

cross-dispersion axis for each wavelength. As the average scan length for each image is about 170 pixels, we chose a slightly smaller aperture to minimize potential edge effects of the scan. However, using slightly smaller and larger apertures (162 pixels and 172 pixels) made no notable improvements to the results.

Across the five visits, there is less than a 0.2 pixel shift in both the x - and y -directions of the scan. A comparison of the residuals, created by subtracting off the best-fit models, to their corresponding x - and y -shifts demonstrated no correlation. We therefore did not apply any correction to these small shifts. We also found no correlation with either the scan length or background values to the residuals.

Due to the crowded stellar field, we checked the Gaia catalog for nearby bright sources. Two stars lie within 5 arcseconds of GJ 1132, one with a Gaia-listed r_p -magnitude of 16.18 and the other of 16.82 (Gaia Collaboration et al. 2016, 2021). With an r_p -magnitude of 10.9, GJ 1132 is more than $130\times$ brighter than these stars. However, one of these faint stars presents as a weak 0.5% background source contaminating the GJ 1132 spectrum for each read, as similarly noted in Mugnai et al. (2021). This background source contamination imparts a 12 ppm systematic suppression of the overall transit depth, smaller than the 34 ppm wavelength-binned spectroscopic transit depth uncertainties. Moreover, a comparison of the average spectrum between visits demonstrated less than a 1% flux variation across all wavelengths (Figure 1), as expected from Gaia.

Comparing each visit’s absolute flux to the global median-combined total flux spectrum shows $< 0.2\%$ deviation for visits 2–5 across 1.15 to $1.63 \mu\text{m}$ (Figure 2). Visit 1 demonstrates a $< 0.8\%$ deviation with larger divergence at shorter wavelengths. This difference between the visits is likely a stellar effect. Visits 1 and 2 were observed 158 days apart ($1.2\times$ the stellar rotation rate of 130 days) while visits 2–5 were all observed within 64 days of one another ($0.5\times$ the stellar rotation). To mitigate the slight flux variation across all visits, we opted to analyze each visit independently, as discussed in further detail below.

3. Analysis

We analyzed the WFC3 data both as wavelength-integrated broadband light curves and as binned spectroscopic light

¹³ <https://github.com/ucl-exoplanets/Iraclis>

¹⁴ <http://astroutils.astronomy.ohio-state.edu/time/>

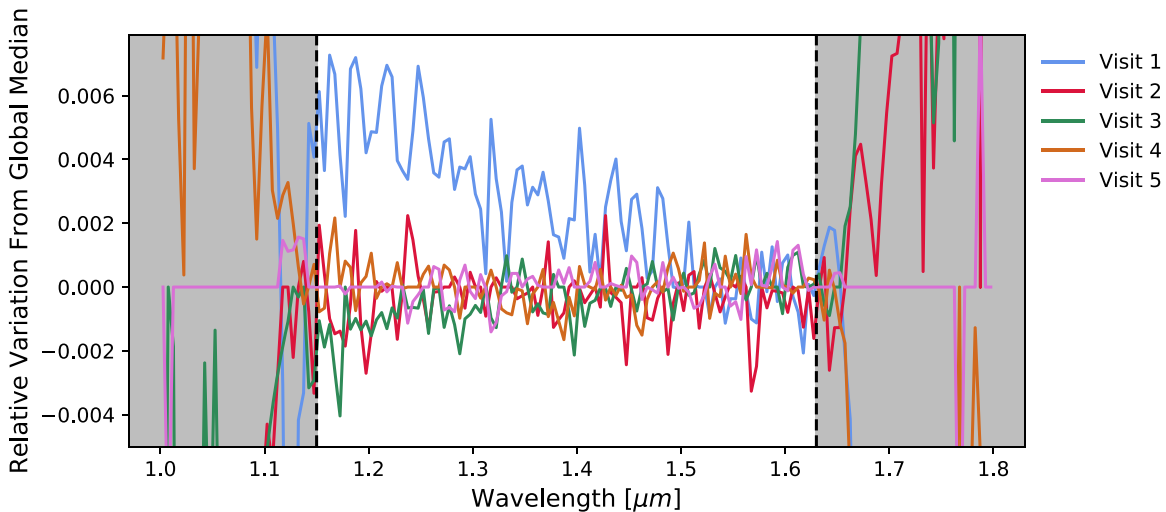


Figure 2. The deviation of each visit from the global medium-combined stellar spectrum created from the combination of all five visits. Visits 2–5 show $<0.2\%$ difference across $1.15 \mu\text{m}$ and $1.63 \mu\text{m}$, while Visit 1 differs by $<0.8\%$, most notably at shorter wavelengths. Dashed lines highlight the high-S/N region.

curves. We also examined archival TESS data of GJ 1132, enabling both a new optical transit depth for GJ 1132b and a search for transits of the radial-velocity detected planet GJ 1132c (Bonfils et al. 2018).

3.1. HST Broadband Light-curve Analysis

From the *iraclis*-reduced spectra, we created broadband light curves for each visit by summing the flux from 1.15 to $1.63 \mu\text{m}$. Uncertainties are a combination of the photon shot noise from the star, sky background, dark current, and read noises added in quadrature. As observed in multiple WFC3 light curves, each orbit demonstrated charge-trapping ramps, with the first orbit exhibiting significantly larger effects (e.g., Berta et al. 2012; Kreidberg et al. 2014; Wakeford et al. 2016; Zhou et al. 2017). We multiplied the physical charge-trapping instrumental model RECTE (Zhou et al. 2017) with the BATMAN transit model (Kreidberg 2015) and fitted each visit independently across all parameters (including both transit and instrumental systematic parameters).

For the RECTE portion of the model, we fitted for the starting number of slow and fast traps ($E_{s,f}$) as well as the number of traps between the orbits for slow and fast traps ($\Delta E_{s,f}$) recommended by Zhou et al. (2017). We also discovered that fitting for the total number of slow and fast traps ($E_{s,\text{tot}}$ and $E_{f,\text{tot}}$) significantly improved the fits for each visit. This is in contrast to Zhou et al. (2017), who recommended holding the total number of traps, trapping times, and trapping efficiencies constant. We found that varying trapping times and efficiencies did not improve our overall fits, and held these constant to the values listed in Zhou et al. (2017). We included visit-long slopes and flux offsets to the charge-trapping model, with these parameters dependent on the scanning direction. While Zhou et al. (2017) note that one benefit of RECTE is the inclusion of the first orbit, we discovered that removing this orbit improved the overall fits for the three remaining orbits. Guo et al. (2020) also found this to be true in their WFC3 analysis of HD 97658b. RECTE is designed to approximate the charge trapping occurring per pixel. We therefore assumed an average per-pixel flux value by dividing the total flux in an image by the number of pixels

contained in the aperture before fitting the systematics with RECTE.

For the BATMAN transit portion of the model, we performed two independent versions of the transit fit: (1) varying a/R_s and inclination and (2) holding these two parameters constant to the values determined by Dittmann et al. (2017) from high-cadence Spitzer data. For both versions, we fitted for the mid-transit time and R_p/R_s . Each visit only sampled the ingress or egress of the transit, and therefore we held the quadratic limb-darkening coefficients constant. These values were determined by LDTK (Parviainen & Aigrain 2015) in the WFC3 bandpass using GJ 1132’s stellar parameters: $\log g = 5.049$ (Dittmann et al. 2017), $Z = -0.12$ and $T_{\text{eff}} = 3270 \text{ K}$ (Berta-Thompson et al. 2015). The period remained fixed to that determined by Dittmann et al. (2017). We held the eccentricity constant at 0, which is supported by previous RV measurements from Berta-Thompson et al. (2015) and Bonfils et al. (2018). We also integrated the transit model over the WFC3 total exposure time of 103 seconds; accounting for this finite integration time is particularly important because it is comparable to the ingress/egress time (see Kipping 2010).

Our combined RECTE and BATMAN model for the flux $F_{\text{for,rev}}(t)$ as a function of both the forward and reverse scan direction over time t is therefore:

$$F_{\text{for,rev}}(t) = (F_{\text{for,rev}} + m_{\text{for,rev}}t) \times \text{RECTE}(E_{s,f}, \Delta E_{s,f}, E_{s_{\text{tot}}}, E_{f_{\text{tot}}}) \times \text{BATMAN}(R_p/R_s, t_0, (a/R_s)^{\text{ver}}, i^{\text{ver}}). \quad (1)$$

$F_{\text{for,rev}}$ and $m_{\text{for,rev}}$ represent the initial offset and visit-long slope for the forward and reverse scanning directions, respectively. Parameters denoted with $\{s, f\}$ in the RECTE model refer to slow and fast trap parameters, respectively, and parameters with ‘ver’ depend on the transit version in question. These parameters, combined with an error-scaling parameter, lead to 15 and 13 fitted parameters for the first and second versions, respectively.

We used *emcee* (Foreman-Mackey et al. 2013) to fit the above model to each of the five visits separately. An error-scaling term (f_{scale}) was multiplied to the flux uncertainties in order for the MCMC to inflate the errors to achieve $\chi_r^2 = 1$.

Table 1
Best-fit Parameters for GJ 1132b across the Five HST Visits and the Folded TESS Light Curve

	Visit 1	Visit 2	Visit 3	Visit 4	Visit 5	TESS
——version 1: a/R_s and i free parameters——						
Mid-transit Time (T_0) (-2457000 BJD)	862.19219 ± 0.00051	1020.20402 ± 0.00327	1077.21000 ± 0.00054	1080.46869 ± 0.00007	1083.72525 ± 0.00090	1544.71753 ± 0.00037
R_p/R_s	0.05035 ± 0.00074	0.04969 ± 0.00076	0.04969 ± 0.00076	0.04981 ± 0.00058	0.04867 ± 0.00083	0.04913 ± 0.00130
a/R_s	$13.61^{+3.15}_{-0.79}$	$11.02^{+2.32}_{-1.60}$	$16.65^{+0.68}_{-1.27}$	$16.47^{+0.77}_{-1.30}$	$17.59^{+1.69}_{-2.55}$	$16.57^{+0.35}_{-0.93}$
i (deg)	$87.34^{+2.10}_{-0.40}$	$88.22^{+1.27}_{-1.81}$	89.26 ± 0.81	88.91 ± 0.74	$89.19^{+0.56}_{-1.16}$	$89.33^{+0.47}_{-0.73}$
f_{scale}	1.29 ± 0.11	1.17 ± 0.10	1.24 ± 0.12	1.19 ± 0.10	1.21 ± 0.11	1.19 ± 0.01
χ_r^2 (dof)	2.29 (51)	1.73 (49)	2.57 (50)	2.12 (51)	2.23 (51)	1.42 (19017)
——version 2: fixed a/R_s : 16.54 i : 88.68——						
Mid-transit Time(T_0) (-2457000 BJD)	862.19257 ± 0.00006	1020.19808 ± 0.00004	1077.21151 ± 0.00005	1080.46896 ± 0.00004	1083.72617 ± 0.00005	1544.71367 ± 0.00011
R_p/R_s	0.04943 ± 0.00024	0.04901 ± 0.00023	0.04901 ± 0.00023	0.04905 ± 0.00035	0.04860 ± 0.00025	0.05021 ± 0.00074
f_{scale}	1.19 ± 0.10	1.21 ± 0.11	1.11 ± 0.10	1.32 ± 0.12	1.23 ± 0.11	1.15 ± 0.01
χ_r^2 (dof)	2.00 (53)	1.58 (51)	1.79 (52)	2.09 (53)	2.18 (53)	1.33 (19019)

Uniform priors were assumed for all parameters. We assigned 100 walkers with 100,000 steps. After an initial run, we checked for any outliers that fell $>5\sigma$ away from the median absolute deviation (MAD). These points were flagged and removed, and the fit was performed again. This accounted for two outlier points in Visit 2 and one outlier point in Visit 3. We binned the residuals from this fit and found a $1/\sqrt{N}$ Gaussian slope, demonstrating that we properly isolated and removed correlated noise. We also checked for parameter convergence by calculating the autocorrelation length using the method presented in Hogg & Foreman-Mackey (2018). A visual inspection of each parameter shows convergence is achieved after 10,000 steps per walker, though we discard the first 50,000 steps as burn-in. This left >500 independent samples left per posterior for analysis.

We decided to perform the two versions noted above, as the transit duration of each visit is largely unconstrained. By varying a/R_s and inclination for the first fit, we determined that all visits have less than a 2σ deviation from those values quoted in Dittmann et al. (2017). Therefore, we adopted the Dittmann et al. (2017) values for these parameters (a/R_s : 16.54 i : 88.68 $^\circ$) for our second fit. By holding a/R_s and inclination constant, we determined a more precise R_p/R_s and mid-transit time, though there is little deviation in the overall value between the two versions for both parameters. Table 1 lists our best-fit planetary parameters from both versions for the five HST visits. The second version parameters were then used for all further analyses, including the transmission spectrum analysis in Section 3.2. We included the parameters determined from the TESS light curve (Section 3.3) to Table 1 for comparison. The error-scaling parameter (f_{scale}) and χ_r^2 are listed as goodness-of-fit measurements.

We calculated the stellar density using the a/R_s from each broadband transit and found that those of all but Visit 2 were within 1σ of the $29.6 \pm 6.0 \text{ g cm}^{-3}$ reported in Berta-Thompson et al. (2015). Visit 2 has the least number of points defining the ingress or egress, making it a challenge to constrain the transit duration (and therefore stellar density). Southworth et al. (2017) measured a lower stellar density of $15.4^{+4.8}_{-3.4} \text{ g cm}^{-3}$, which gave them larger stellar and planetary radii; we find that all of our visits except for 1 and 2 have a $>2\sigma$ deviation from

this value. We therefore opt to use the stellar and planetary radii derived in Berta-Thompson et al. (2015) and Bonfils et al. (2018).

We plotted the five broadband light curves with the best-fit models from the second version (assuming constant a/R_s and inclination) in Figure 3. From the top down, each panel shows: the normalized flux, the transit with the RECTE model removed, the systematics with the BATMAN transit model removed, and the residuals. Visit 1 has the largest deviation in flux between the forward and reverse scans, giving the ramp an up-and-down motion that is not as apparent in the other four visits. The origin of this difference is unclear, though the systematics model captures this effect. We do not plot the best fit from the first version (varying a/R_s and inclination), as the differences between the fits are slight and not apparent when plotted against each other.

3.2. HST Spectroscopic Light-curve Analysis

We created 22 spectroscopic light curves by summing the flux between 1.15 to 1.63 μm into five-pixel bins (approximately 20 nm each). We analyzed these light curves using two different methods: fitting each light curve using RECTE and using the broadband divide-white method described in Kreidberg et al. (2014).

RECTE Model—We again approximated a per-pixel average by dividing the total summed flux in the spectroscopic channel by the number of pixels in the smaller binned aperture. Similar to the broadband light-curve analysis, we did not include the first orbit. We included the number of slow and fast traps as fitted parameters. LDTK was used to determine the quadratic limb-darkening parameters for each wavelength bin, which were held constant throughout each individual fit. a/R_s and inclination were held constant to the Dittmann et al. (2017) values. The mid-transit time was held constant to that obtained from the second-version WFC3 broadband fit. This left R_p/R_s as the only free transit model parameter, along with the 10 systematic parameters from the RECTE model and an error-scaling term.

Every spectroscopic light curve for each visit was modeled individually with the same emcee MCMC process as the

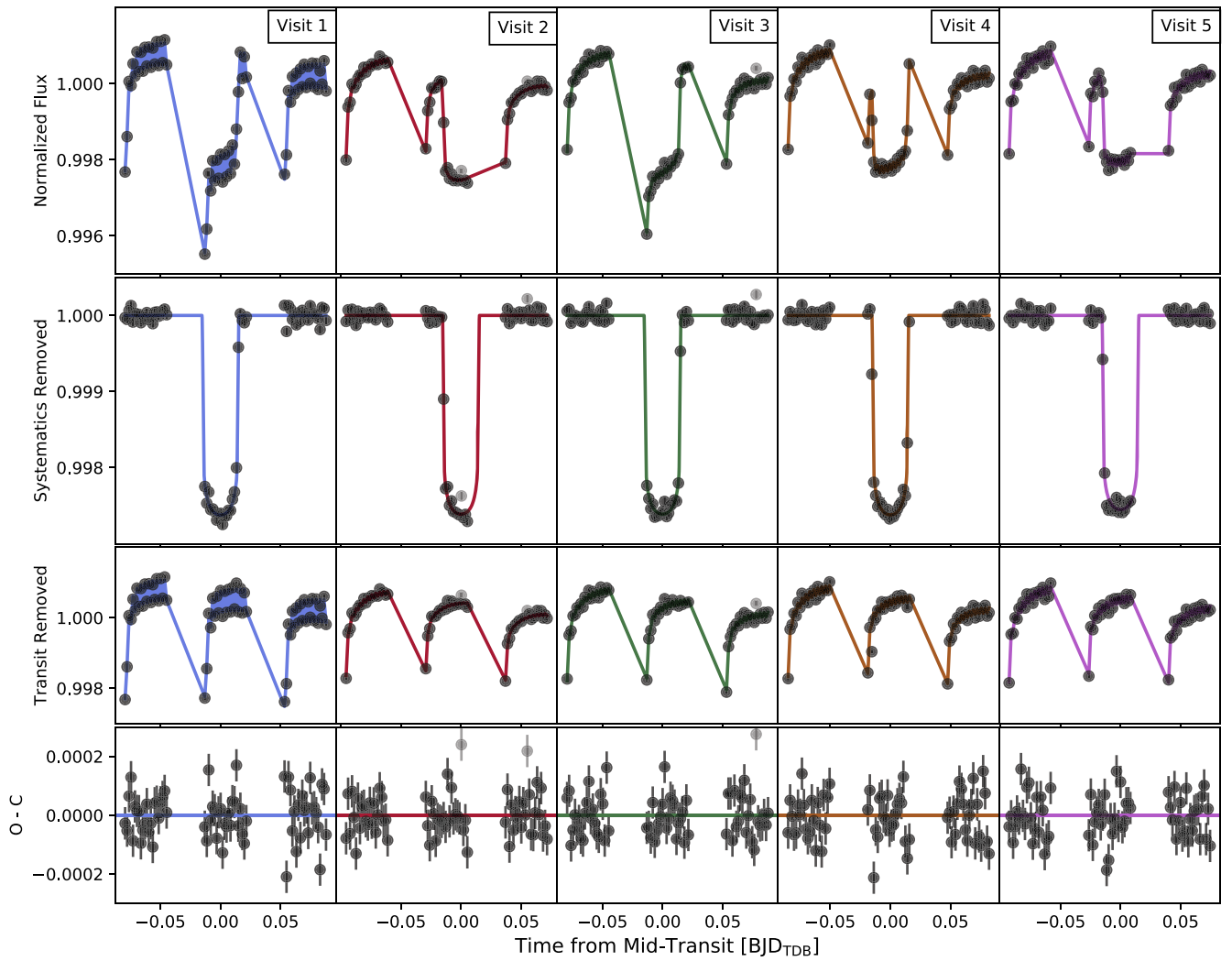


Figure 3. Broadband light curves for each WFC3 transit of GJ 1132b, with each visit plotted left to right, including the raw light curves with transit and ramp-like systematics (*first row*), the transits with the RECTE systematic model divided out (*second row*), the systematics with the BATMAN transit model divided out (*third row*), and the final residuals (*fourth row*). Outlying points are noted as light gray points.

broadband curves. The R_p/R_s for each visit and the corresponding wavelength bins are noted in Table 2. Inverse-variance weighted averages calculated from the five visits are listed in the last column of the table. Each spectroscopic light curve for the five visits is plotted in Figure 4, with the systematics-removed transit curve plotted on the left and the residuals for each bin to the right. We find little deviation in the RECTE model parameters from bin to bin, highlighting their mostly wavelength-independent nature.

Divide-white Method—We checked our RECTE analysis by applying the divide-white method to the spectroscopic light curves (Kreidberg et al. 2014). We created systematic residuals (third row in Figure 3) by dividing the broadband transit model from the broadband data. By assuming these systematic residuals are not wavelength-dependent, we divided these residuals from each spectroscopic light curve. We found that, while the residuals captured the ramp-like effect of the data, they do not necessarily remove the difference in the forward and backward scanning offset. We therefore fit for two separate offsets, dependent on the scanning direction, as well as the transit depth and an error-scaling term. Again, we performed the same emcee MCMC routine as for the broadband and RECTE analyses discussed above.

A comparison of the inverse-weighted combined transit depths between the RECTE and divide-white methods demonstrated discrepancies that were $<2\sigma$ for all but the second wavelength bins (Figure 5). The RECTE method always produced slightly larger error bars on the transit depths due to the larger number of free parameters. We opted to use the RECTE transit depths $(R_p/R_s)^2$ for the rest of the analysis and discussion in this paper, as this model is based on physical properties of the detector.

3.3. TESS Light-curve Analysis of GJ 1132b

GJ 1132 was observed by TESS during Sectors 9 and 10, and again in Sector 36. In Sector 10, the star appeared on a noisier section of the CCD, thus demonstrating larger instrumental variation. We therefore removed Sector 10 from this analysis, which led to a total of 28 transits split between Sectors 9 and 36. We used the Python package `lightkurve` (Lightkurve Collaboration et al. 2018) to download and analyze the two-minute-cadence observations in Sector 9 and the 20-second-cadence observations in Sector 36. Starting from the PDC light curve, we detrended the flux by masking out all GJ 1132b transits and applying a median

Table 2
The R_p/R_s for Each Wavelength Bin across Each Visit

Wavelength [μm]	Visit 1	Visit 2	Visit 3	Visit 4	Visit 5	Weighted Average
1.150–1.172	0.04798 \pm 0.00091	0.05072 \pm 0.00109	0.04965 \pm 0.00099	0.04947 \pm 0.00074	0.04916 \pm 0.00085	0.04931 \pm 0.00040
1.172–1.194	0.05050 \pm 0.00089	0.04891 \pm 0.00077	0.05044 \pm 0.00084	0.04923 \pm 0.00077	0.04760 \pm 0.00085	0.04930 \pm 0.00037
1.194–1.215	0.04952 \pm 0.00080	0.04929 \pm 0.00080	0.04877 \pm 0.00096	0.05018 \pm 0.00079	0.04992 \pm 0.00076	0.04960 \pm 0.00036
1.215–1.237	0.04897 \pm 0.00071	0.04880 \pm 0.00074	0.05021 \pm 0.00077	0.04836 \pm 0.00065	0.04908 \pm 0.00081	0.04902 \pm 0.00033
1.237–1.259	0.04948 \pm 0.00069	0.04912 \pm 0.00072	0.04737 \pm 0.00052	0.05004 \pm 0.00080	0.04972 \pm 0.00081	0.04881 \pm 0.00030
1.259–1.281	0.04924 \pm 0.00084	0.04786 \pm 0.00081	0.04941 \pm 0.00078	0.05035 \pm 0.00077	0.04920 \pm 0.00074	0.04923 \pm 0.00035
1.281–1.303	0.04959 \pm 0.00063	0.04955 \pm 0.00077	0.04915 \pm 0.00071	0.04948 \pm 0.00063	0.04695 \pm 0.00087	0.04912 \pm 0.00032
1.303–1.324	0.04868 \pm 0.00062	0.05022 \pm 0.00065	0.04964 \pm 0.00059	0.05128 \pm 0.00075	0.04949 \pm 0.00070	0.04977 \pm 0.00029
1.324–1.346	0.04935 \pm 0.00072	0.05091 \pm 0.00068	0.04843 \pm 0.00081	0.05028 \pm 0.00082	0.04861 \pm 0.00077	0.04959 \pm 0.00034
1.346–1.368	0.04885 \pm 0.00060	0.04821 \pm 0.00083	0.05005 \pm 0.00077	0.04934 \pm 0.00069	0.04868 \pm 0.00072	0.04903 \pm 0.00032
1.368–1.390	0.04823 \pm 0.00079	0.05009 \pm 0.00087	0.04897 \pm 0.00071	0.04971 \pm 0.00070	0.04914 \pm 0.00078	0.04921 \pm 0.00034
1.390–1.412	0.05095 \pm 0.00072	0.04959 \pm 0.00099	0.04949 \pm 0.00068	0.04790 \pm 0.00058	0.05064 \pm 0.00085	0.04947 \pm 0.00033
1.412–1.433	0.05025 \pm 0.00091	0.04808 \pm 0.00072	0.04855 \pm 0.00061	0.04769 \pm 0.00091	0.04771 \pm 0.00085	0.04848 \pm 0.00034
1.433–1.455	0.04914 \pm 0.00080	0.04874 \pm 0.00080	0.05050 \pm 0.00084	0.04879 \pm 0.00091	0.04803 \pm 0.00076	0.04893 \pm 0.00037
1.455–1.477	0.05045 \pm 0.00091	0.04813 \pm 0.00085	0.05062 \pm 0.00076	0.04897 \pm 0.00077	0.04849 \pm 0.00074	0.04930 \pm 0.00036
1.477–1.499	0.05066 \pm 0.00075	0.04965 \pm 0.00075	0.04956 \pm 0.00075	0.04850 \pm 0.00083	0.04930 \pm 0.00080	0.04958 \pm 0.00035
1.499–1.521	0.04972 \pm 0.00078	0.04996 \pm 0.00092	0.04909 \pm 0.00070	0.04819 \pm 0.00074	0.04884 \pm 0.00074	0.04908 \pm 0.00034
1.521–1.542	0.05029 \pm 0.00071	0.04971 \pm 0.00069	0.05018 \pm 0.00100	0.04944 \pm 0.00071	0.04962 \pm 0.00075	0.04981 \pm 0.00034
1.542–1.564	0.04926 \pm 0.00083	0.04935 \pm 0.00089	0.04987 \pm 0.00077	0.05148 \pm 0.00081	0.04821 \pm 0.00080	0.04964 \pm 0.00037
1.564–1.586	0.04970 \pm 0.00083	0.04729 \pm 0.00088	0.04971 \pm 0.00079	0.04895 \pm 0.00079	0.04963 \pm 0.00067	0.04915 \pm 0.00035
1.586–1.608	0.04963 \pm 0.00079	0.04888 \pm 0.00086	0.04958 \pm 0.00081	0.04845 \pm 0.00086	0.04789 \pm 0.00087	0.04891 \pm 0.00038
1.608–1.630	0.04991 \pm 0.00103	0.04857 \pm 0.00084	0.04972 \pm 0.00084	0.04979 \pm 0.00071	0.04736 \pm 0.00075	0.04900 \pm 0.00036

Notes. We include the inverse-variance weighted average of the visits in the last column. To reproduce the transit depths plotted throughout this paper, we use $(R_p/R_s)^2$ as the transit depth and $2(R_p/R_s)\sigma_{R_p/R_s}$ to calculate the transit depth uncertainty.

(This table is available in machine-readable form.)

moving boxcar filter with a baseline of one day ($32\times$ the transit duration). As with the broadband WFC3 transits, we performed the same two versions of fits as above (varying a/R_s and inclination and holding them constant) to all transits simultaneously. We include a baseline of 135 minutes ($3\times$ the transit duration) on either side of each transit. For both versions, we fitted for R_p/R_s , transit ephemeris, as well as a general offset. We assumed uniform priors on all parameters, including an error-scaling term. We also fitted for the quadratic limb-darkening coefficients using the parameterization method discussed in Kipping (2013) and assigning q_1 and q_2 uniform priors from 0 to 1. Table 1 lists the best-fit parameters for both versions, and Figure 6 plots the best-fit model atop the folded data. We found no significant difference between the two versions; the fitted values of a/R_s and inclination were consistent with those from Spitzer (Dittmann et al. 2017).

Due to the large pixel size, the stellar flux measured by TESS may experience dilution if not properly accounted for. GJ 1132 is assigned a TIC dilution coefficient of 12.1%. However, we used the PDCSAP flux downloaded with `lightkurve`, which should already be dilution-corrected. We check the TESS derived transit depth with the depth determined by MEarth (Section 4.1.3), which covers a similar bandpass, and find no significant depth difference between the two instruments. We are therefore confident that the pixel dilution was properly accounted for.

We analyzed the individual TESS transits, again applying the two versions. Using the a/R_s and inclination values for each transit, we calculated the transit duration for each epoch. We see no evidence for transit duration variations or transit depth variations in the data for TESS Sectors 9 and 36. A brief

inspection of Sector 10 showed large variations in each, due to significant uncorrected instrumental noise in the data even after the median detrending, supporting our decision to remove this sector from our analysis.

We measured the mid-transit times for each transit in Sectors 9 and 36, holding a/R_s and inclination constant. We combined these times with the broadband mid-transit times for each HST visit as well as the published times from MEarth (Berta-Thompson et al. 2015; Dittmann et al. 2017), Spitzer (Dittmann et al. 2017), and the MPG telescope (Southworth et al. 2017). Diamond-Lowe et al. (2018) noted that their mid-transit times for GJ 1132b were consistently 2 minutes early for all four of their observed transits, and they were unable to determine the cause of this difference. We also observed this discrepancy, and we do not include their times for our analysis. The uncertainties on the mid-transit times determined from the WFC3 observations are on the order of four seconds, much less than the exposure time of one data point. To more cautiously capture this uncertainty, we modeled a straight line through only the five HST times, inflating their errors such that the reduced χ^2 of this linear model equaled 1. This required us to inflate the HST uncertainties by a factor of 10.7, which we applied to the rest of the transit times analysis. Using the BJD_{TDB} mid-transit times for each epoch, we fit a straight line through these points, providing an updated period of $1.6289299 \pm 2 \times 10^{-7}$ days and a transit ephemeris of $2457184.55747 \pm 0.00011 \text{ BJD}_{\text{TDB}}$. Table 3 reports the mid-transit times for HST broadband curves with the inflated uncertainties and times from Sectors 9 and 36 of TESS. A search for transit timing variations (TTVs) yielded a nondetection, with the residuals matching a flat line with $\chi^2_{\text{r}} = 1.36$ for 67 degrees of freedom (Figure 7).

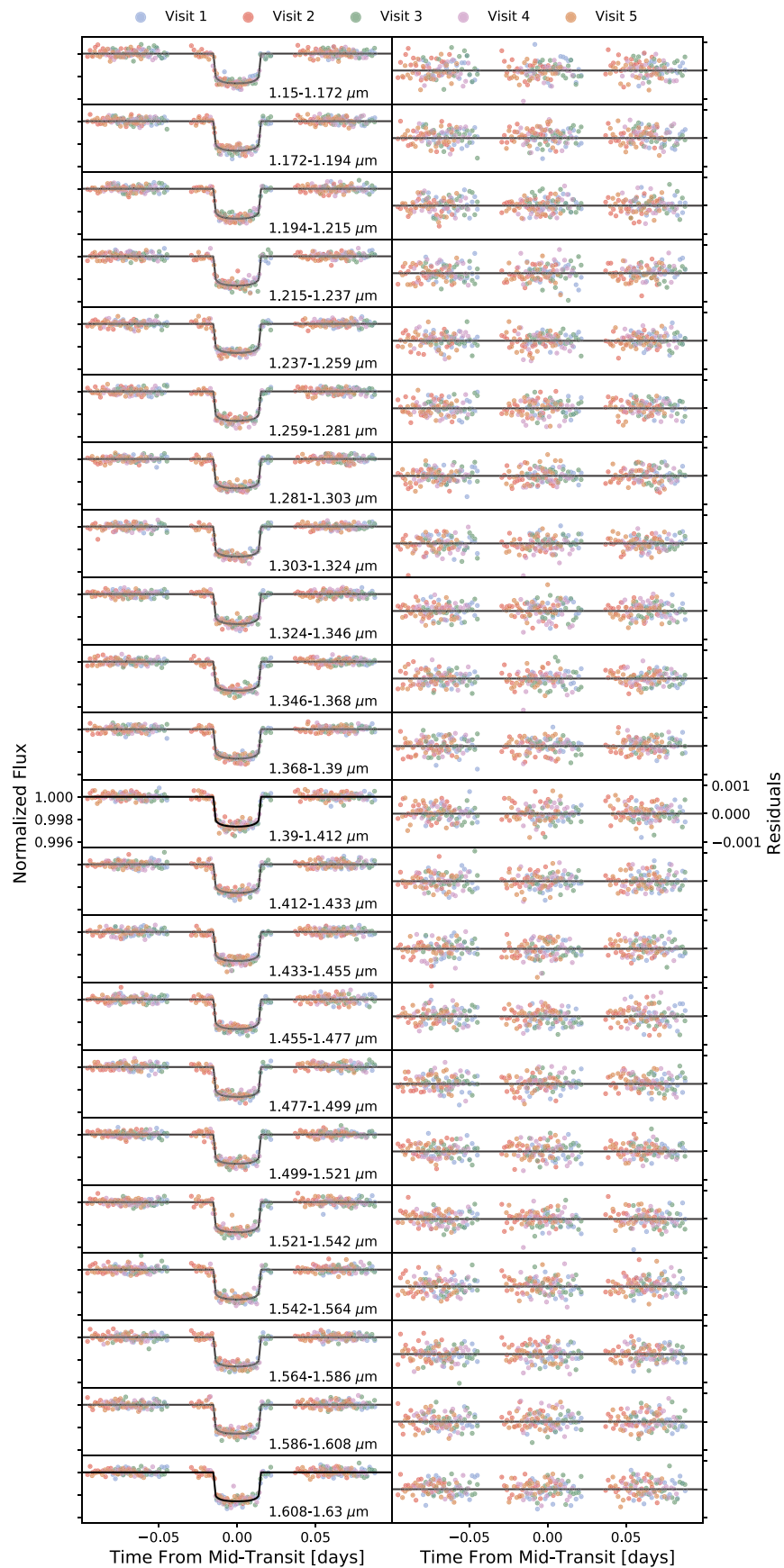


Figure 4. Each of the 22 spectroscopic light curves plotted with the smallest to largest wavelength bins being arranged from top to bottom. Point colors correspond to one of the five visits. Light curves are shown with systematics removed and with the transit model created from the weighted-average transit depth of the five visits (*left*), and residuals from this shared model are shown (*right*).

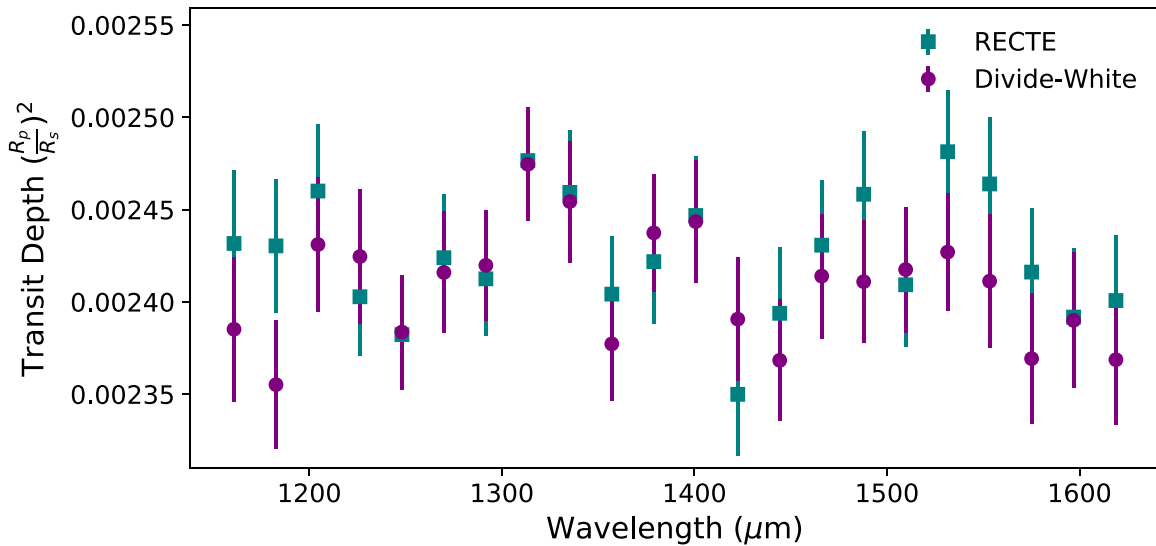


Figure 5. A transit depth comparison between the RECTE (teal/square) and divide-white (purple/circle) methods for each wavelength bin. Overall, transit depths vary less than 2σ for each bin (except for the second bin) with an average discrepancy of less than 1σ .

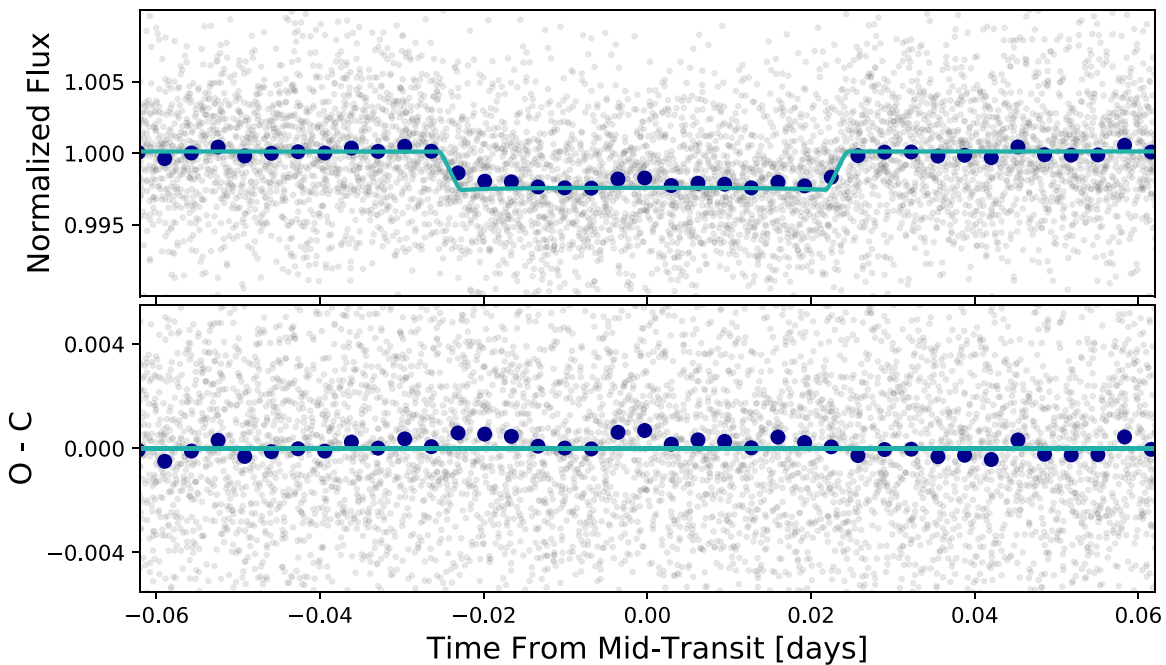


Figure 6. TESS folded light curve of GJ 1132b's transit. Top panel includes the detrended light curve points (gray), binned points for clarity (blue), and the best-fit model in light blue. Bottom panel shows the residuals from this fit.

3.4. TESS Light-curve Analysis of GJ 1132c

Discovered with radial velocities by Bonfils et al. (2018), GJ 1132c has not yet been completely vetted for the possibility of transits. Bonfils et al. (2018) estimate a 1% transit probability. No obvious transits were seen in MEarth or Spitzer data, but they lacked complete and continuous coverage of the possible times of transit. We use TESS's continual coverage to search for the possibility of a GJ 1132c transit. We predict two possible transit events of GJ 1132c to occur in Sector 9 and 36. We masked out all GJ 1132b transits in the median boxcar detrended data. We assumed Gaussian priors on the a/R_s , mid-transit time and period parameters using values determined by Bonfils et al. (2018), and set uniform priors on R_p/R_s and the inclination. We allow for grazing transits by letting the impact

parameter to vary from 0 to $1 + R_p/R_s$. We also allow for the possibility of negative transit depths. The quadratic limb-darkening coefficients were held constant to those values determined from the GJ 1132b TESS fits.

We performed an MCMC fit using 100 walkers and 15,000 steps with 5,000 of those removed for burn-in. We determined an R_p/R_s of $0.024^{+0.011}_{-0.046}$, a result consistent with zero. A visual inspection of the data shows no indication of an obvious transit (Figure 8). From the posterior, we place a 3σ upper limit on R_p/R_s at 0.081, marginalized over all other parameters. This corresponds to a planet radius of $1.84 R_{\oplus}$. With a minimum mass of $2.64 M_{\oplus}$ (Bonfils et al. 2018), it is possible that this planet possesses a radius smaller than what we can detect with TESS. However, we followed up this search by performing a box least squares (BLS) on both Sectors 9 and 36. GJ 1132b is

Table 3
Individual HST and TESS Sector 9 and 36 Mid-transit Times

Transit Epoch	T_0 (-2457000 BJD _{TDB})	Telescope
416	862.19257 ± 0.00061 ^a	HST
513	1020.19808 ± 0.00047 ^a	HST
548	1077.21151 ± 0.00050 ^a	HST
550	1080.46896 ± 0.00041 ^a	HST
552	1083.72617 ± 0.00054 ^a	HST
835	1544.71423 ± 0.00108	TESS
836	1546.34264 ± 0.00126	TESS
837	1547.98548 ± 0.00408	TESS
838	1549.60261 ± 0.00136	TESS
839	1551.23019 ± 0.00214	TESS
840	1552.85822 ± 0.00171	TESS
841	1554.48737 ± 0.00095	TESS
843	1557.74480 ± 0.00112	TESS
844	1559.37409 ± 0.00116	TESS
845	1561.00412 ± 0.00104	TESS
846	1562.63245 ± 0.00176	TESS
847	1564.26092 ± 0.00148	TESS
848	1565.89057 ± 0.00085	TESS
849	1567.51841 ± 0.00101	TESS
1288	2282.61811 ± 0.00072	TESS
1289	2284.24715 ± 0.00163	TESS
1290	2285.87585 ± 0.00160	TESS
1291	2287.50658 ± 0.00083	TESS
1292	2289.13361 ± 0.00124	TESS
1293	2290.75838 ± 0.00286	TESS
1293	2292.39270 ± 0.00145	TESS
1296	2295.65369 ± 0.00148	TESS
1297	2297.28080 ± 0.00072	TESS
1298	2298.90982 ± 0.00075	TESS
1299	2300.54086 ± 0.00226	TESS
1300	2302.16574 ± 0.00124	TESS
1301	2303.79345 ± 0.00134	TESS
1302	2305.42355 ± 0.00059	TESS

Note.

^a Uncertainties have been inflated 10.7× the 1 σ value

easily detected at 1.6289 days, which we then mask. Running BLS again does not show any other significant peaks.

From GJ 1132c’s a/R_s (Bonfils et al. 2018), its orbit would need to be inclined to at least 89.88° (1.2° from GJ 1132b’s orbit) in order to transit. While this is close to co-planar with its transiting neighbor, the tight constraint on GJ 1132c’s inclination required for transits makes it more likely that it is inclined such that it does not transit—a statement supported by TESS observations.

4. Transmission Spectrum and Comparison to Atmospheric Models

4.1. Transmission Spectrum

4.1.1. HST/WFC3 Transmission Spectrum

Before combining the five visits into a weighted-average spectrum, we checked that the modeled transit depths in each bin are drawn from the same distribution with no significant outliers. We determined that every individual depth fell within 2 σ of the weighted-average depth in their respective bin, except for the 1.25 and 1.40 μm bins (Figure 9). Both bins showed a 2.2 σ spread, with Visits 3 and 4 yielding the respective outlying points. A comparison between the average transit depths with and without these visits yielded no difference in

our final result. We therefore keep all five visits when calculating the average transit depth for each wavelength bin.

4.1.2. Comparison to Other HST Analyses

Recently, two other papers published analyses of the same HST/WFC3 data set (Swain et al. 2021; Mugnai et al. 2021), reaching two different conclusions. Swain et al. (2021) saw large-amplitude features and inferred a H/He-rich atmosphere with a Rayleigh scattering slope, HCN, and CH₄ absorption indicating the presence of haze. Mugnai et al. (2021) measured a featureless spectrum with transit depths and uncertainties similar to ours. Figure 10 compares the transmission spectrum results of those two analyses to the WFC3 transmission spectrum that we measure here. Our inferred transit depths disagree strongly with those from Swain et al. (2021) and closely align with those from Mugnai et al. (2021). All three of these works use different approaches to analyze and fit the same underlying data. Both our work and Mugnai et al. (2021) utilize the *iraclis* pipeline to reduce and create light curves from the data. While Mugnai et al. (2021) use an analytical model to quantify the ramp-like systematics, we have chosen to focus on the flexible, physically motivated RECTE model for instrumental systematic parameterization. The similarities in the transit depths indicate that the choice of systematics model does not significantly change the resulting spectrum. However, for our work to match the results from Swain et al. (2021), we would need to introduce systematic noise that precisely offsets the real underlying wave-dependent variation. As this is very unlikely, we conclude that the transmission spectrum of GJ 1132b is effectively flat to 34 ppm precision across the WFC3/G141 bandpass.

4.1.3. Comparison to Other Archival Data

We compared the WFC3 transit depths with archival data along with the broadband TESS point derived in Section 3.3. For each data set, we provide a brief summary below:

1. Dittmann et al. (2017) observed 21 transits of GJ 1132b with MEarth and two transits with the 4.5 μm Spitzer channel. They found a Spitzer transit depth 3 σ larger than the optical MEarth depth—a feature they attributed to unocculted starspots. We reanalyzed the MEarth data (see below) and found a transit depth similar to that of the Dittmann et al. (2017) Spitzer depth.
2. We re-examined the 21 MEarth transits reported in Dittmann et al. (2017) by performing a simple Levenberg–Marquardt fitting routine. We fitted for a common R_p/R_s , a/R_s , and impact parameter (b) across all 21 transits. Airmass coefficients for each transit (21 total coefficients) were also allowed to float, as well as 132 magnitude zero points (one for each combination of night, telescope, and meridian side) (Irwin et al. 2018). We held GJ 1132b’s period and transit ephemeris constant to values in Table 3 of Dittmann et al. (2017). The constant limb-darkening parameters were derived from stellar models (Claret et al. 2012) for a star with T_{eff} : 3300K, and $\log(g)$: 5.0 and translated to the MEarth bandpass using the same method described in Irwin et al. (2018). Parameter uncertainties were scaled to account for overdispersion globally rather than individually per night. This reanalysis yielded a deeper transit depth of 0.00246 ± 0.00011 , a 3 σ difference from the shallower

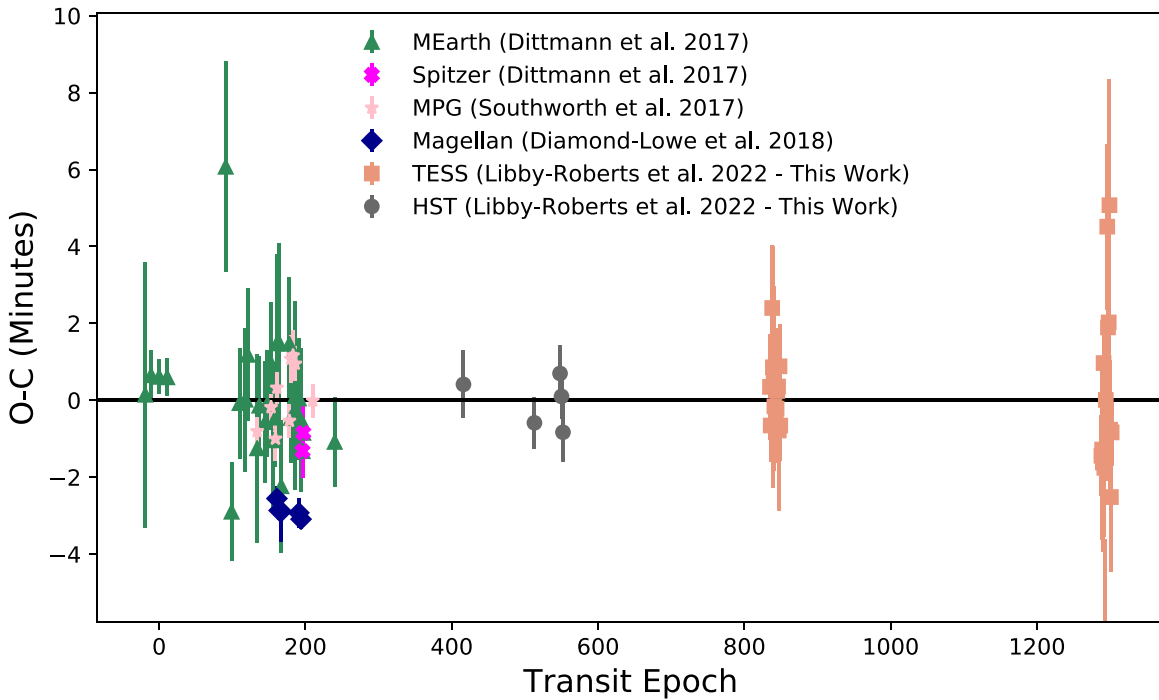


Figure 7. Searching for TTVs in the mid-transit times of GJ 1132b yielded scatter around a flat line. Points are color-coded by telescope, and the HST uncertainties are inflated $10.7\times$ such that the χ_r^2 of those five points is equal to unity.

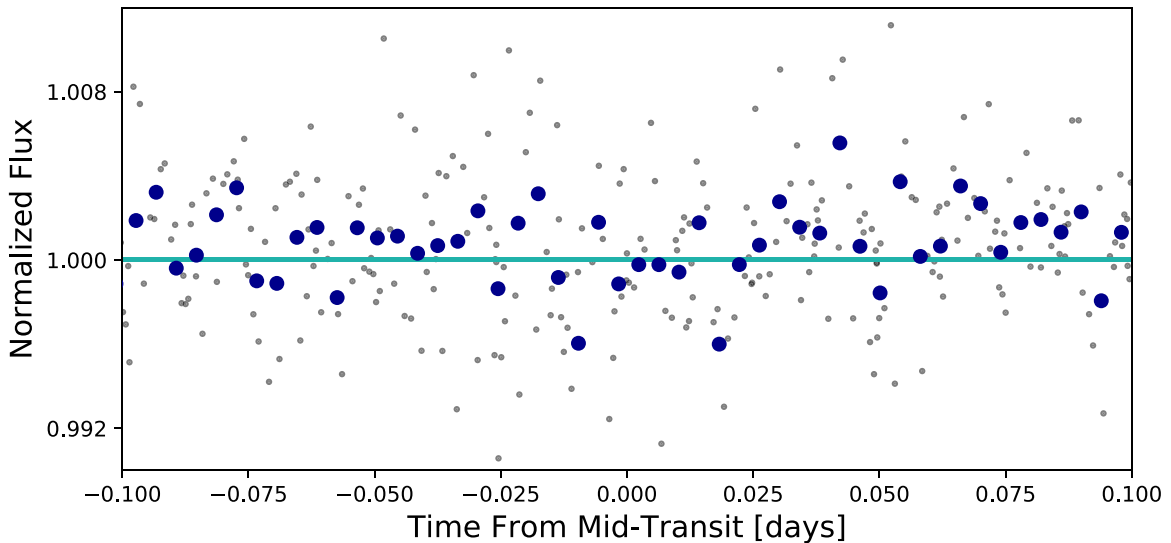


Figure 8. The TESS Sectors 9 and 36 light curve of GJ 1132, folded assuming the best-fit period (8.922 ± 0.009 days) from our TESS analysis of GJ 1132c, with the best-fit maximum-likelihood model plotted in light blue as a straight line. We find no significant evidence that GJ 1132c transits.

transit found in Dittmann et al. (2017). It is statistically the same ($<1\sigma$) as both the Spitzer $4.5\ \mu\text{m}$ and the WFC3 depths. As such, this updated depth indicates no significant stellar contamination between the shorter optical and longer infrared wavelengths.

3. Diamond-Lowe et al. (2018) used the LDSS3C spectrograph on the Magellan Clay telescope to observe the optical spectrum of GJ 1132b from 0.7 to $1.04\ \mu\text{m}$. They found a featureless spectrum and rule out a $1\times$ solar metallicity atmosphere with 3.6σ confidence. However, comparing their transit depths to the WFC3 spectrum depicts a slight offset, with their optical transit depths appearing smaller than those in the infrared. A close

inspection shows that the broadband transit depth reported in Diamond-Lowe et al. (2018) is deeper than any of their spectroscopic depths while also being statistically similar to the depths derived from the WFC3 observations (Figure 11). We hypothesize that this difference is due to instrumental and systematic effects, and is not astrophysical in nature.

4. Southworth et al. (2017) observed nine broadband transits with the GROND instrument on the 2.2 m MPG telescope. They measured larger transit depths in both the z and K bandpasses, which suggested large H_2O or CH_4 absorption in the atmosphere of GJ 1132b. Due to their large transit depth uncertainties and disagreement

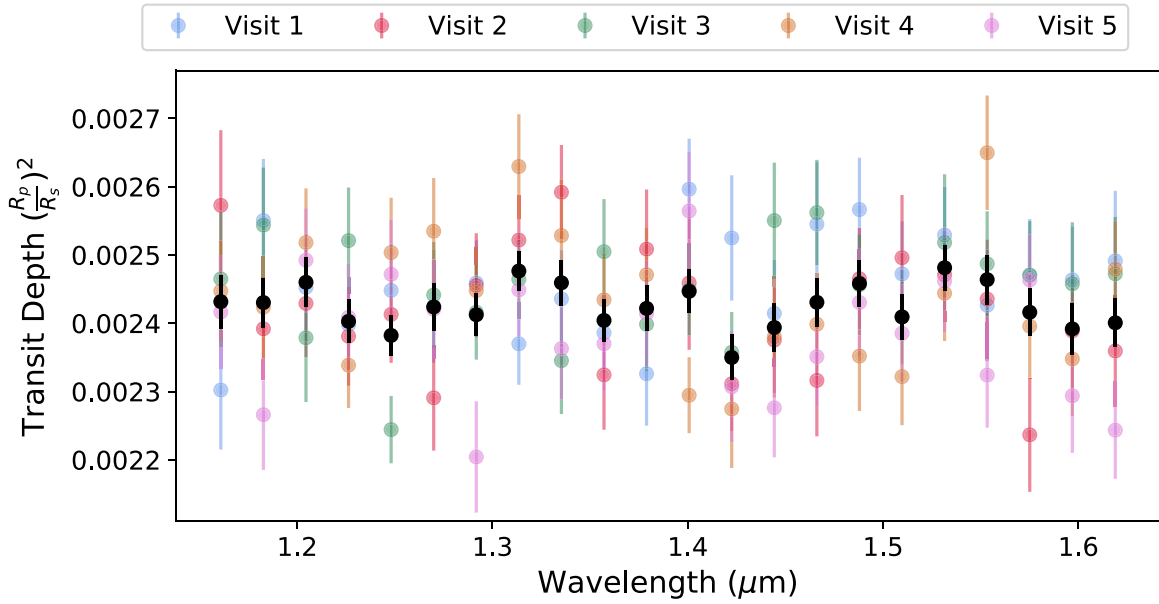


Figure 9. A comparison of the transit depths from each visit in their respective wavelength bins. The weighted-mean transit depths between the five visits are included in black. All bins demonstrated $<2\sigma$ spread, except for wavelengths 1.25 and 1.40 μm . Removing the outlying visits in these bins had no appreciable effect on the final spectrum.

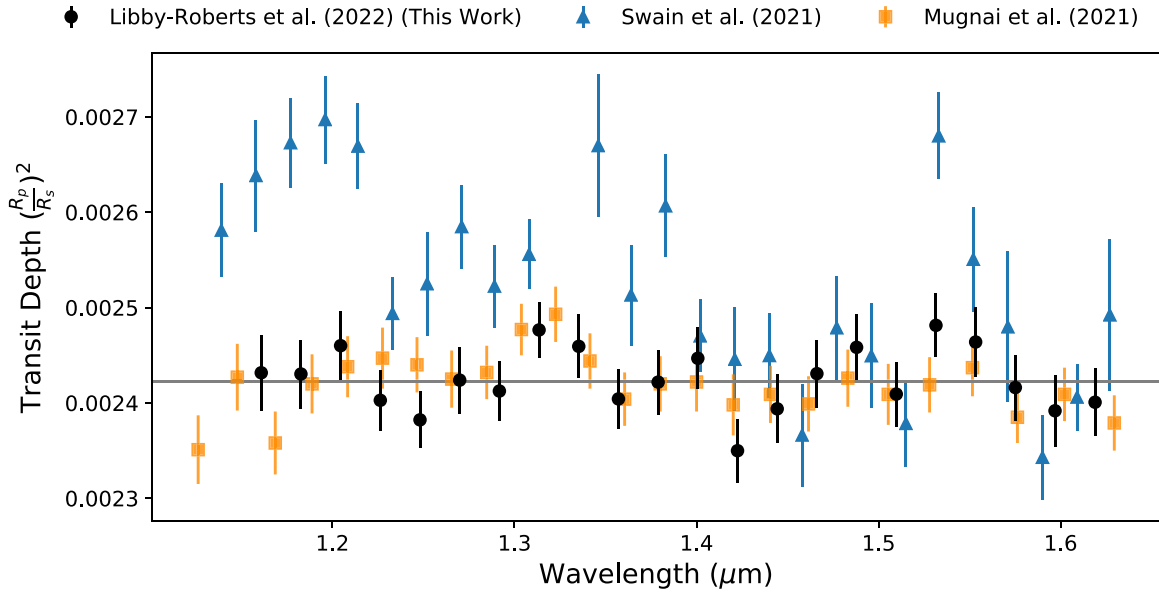


Figure 10. A comparison between the average transit depths in Swain et al. (2021) (blue/triangle points), in Mugnai et al. (2021) (orange/square points), and in this work (black/circle points). All utilize the same HST/WFC3 data, though Swain et al. (2021) determine very different transit depths, most notably at shorter wavelengths. Transit depths derived in this work and in Mugnai et al. (2021) are statistically the same, with similar uncertainties as well.

with other more precise data sets, we did not include the Southworth et al. (2017) broadband points in any of our analyses.

5. Swain et al. (2021) used these HST/WFC3 data to infer a Rayleigh scattering slope and a possible HCN and CH_4 absorption feature. We do not observe this in our analysis, and we use our featureless WFC3 spectrum for the comparison with the other data sets.
6. Mugnai et al. (2021) also used these HST/WFC3 data but determined a featureless transmission spectrum in agreement with our transit depths. Again, we chose to use our WFC3 depths for the rest of the discussion.

4.2. Comparison to Atmospheric Models

4.2.1. Cloud-free Atmospheric Models

We present the WFC3 weighted-average transit depths for GJ 1132b in Figure 12. The planet’s transmission spectrum is best explained by a flat or featureless spectrum with a χ_r^2 of 1.02 with 21 degrees of freedom. The average transit depth uncertainty is 34 ppm per 20 nm wavelength bin. On GJ 1132b, a H/He-dominated atmosphere with a mean molecular weight of $\mu = 2.3$ would have a scale height of 172 km. The WFC3 transit depth uncertainties correspond to an effective resolution of $0.29\times$ this scale height. In turn, this precision corresponds to

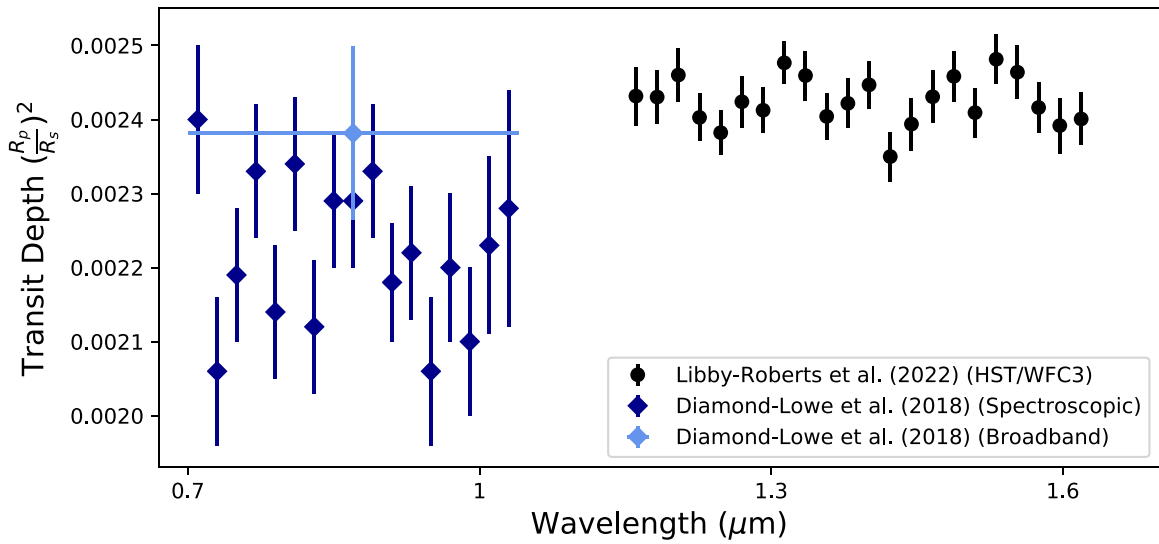


Figure 11. A comparison between the WFC3 transit depths (black points) and the spectroscopic (dark blue) and broadband (light blue) transit depths from Diamond-Lowe et al. (2018). While the spectroscopic depths appear smaller than the WFC3 values, the broadband depth is statistically the same.

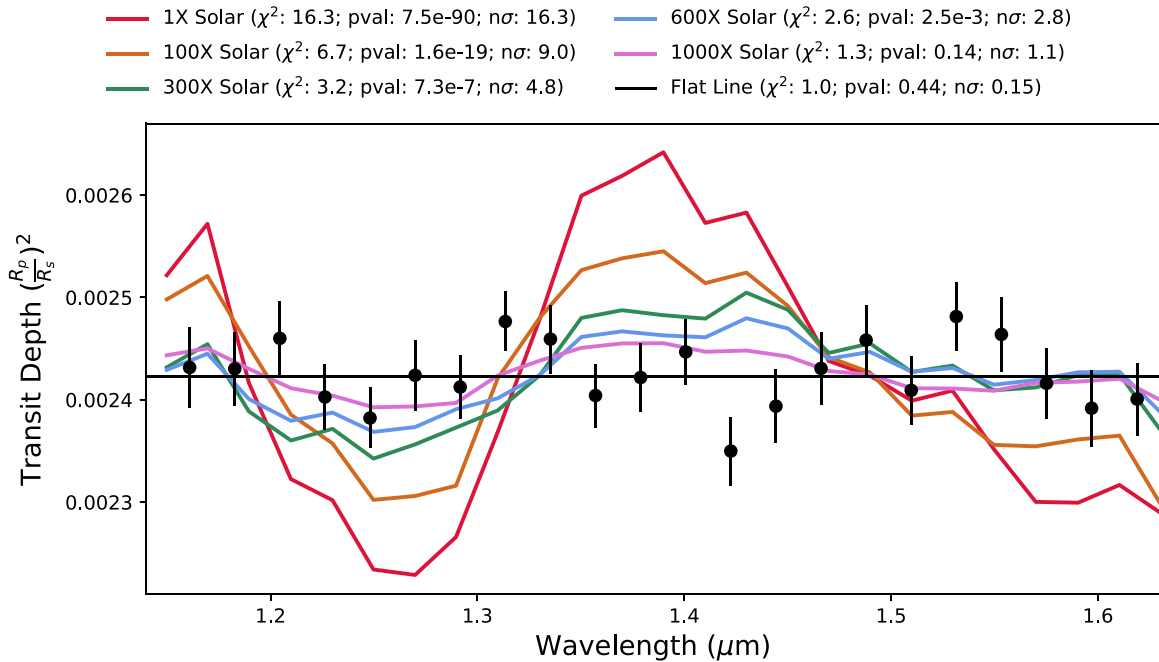


Figure 12. The WFC3 transmission spectrum of GJ 1132b, averaged over the five visits of WFC3, plotted against cloud-free atmospheric models of varying metallicities for comparison. For each model, we provided the χ_r^2 and the p -value evidence against the model. We translated the p -value to the number of σ ($n\sigma$) confidence that we can reject this model. The spectrum is most consistent with a flat line, indicating a high mean molecular weight atmosphere or no atmosphere. We could easily detect an atmosphere with a metallicity less than $300\times$ solar by volume (or mean molecular weights less than 8.9 amu).

one scale height for an atmosphere with $\mu = 7.6$. We expect absorption features in an atmosphere to possess sizes of several scale heights. Based on this precision and the featureless spectrum, we confidently rule out atmospheres with mean molecular weights less than $\mu = 7.6$.

For interpreting these transit depths, we generated model transmission spectra using the original version of Exo-Transmit (Kempton et al. 2017) for atmospheric compositions of $1\times$, $100\times$, $300\times$, $600\times$, and $1000\times$ solar metallicities by volume (Figure 12) as well as atmospheres composed of 100% H_2O , CO_2 , and O_2 (Figure 13). All models were cloud-free and excluded any additional Rayleigh scattering beyond the gaseous species present in the atmosphere. Model pressure–

temperature (P-T) profiles used the custom double-gray profiles (one opacity for shortwave radiation and another opacity for longwave radiation) from Diamond-Lowe et al. (2018). Diamond-Lowe et al. (2018) provide additional details on the calculations of these profiles. Stellar mass and radius values were adopted from Bonfils et al. (2018). As the 1 bar pressure radius is unknown, we used GJ 1132b’s planet radius as a starting point to generate Exo-Transmit models for each metallicity before rescaling the 1 bar radius until the model best fit the HST transmission spectrum (Kempton et al. 2017; Diamond-Lowe et al. 2018).

From the WFC3 observations, we confidently rule out atmospheres with metallicities $<300\times$ solar by volume at

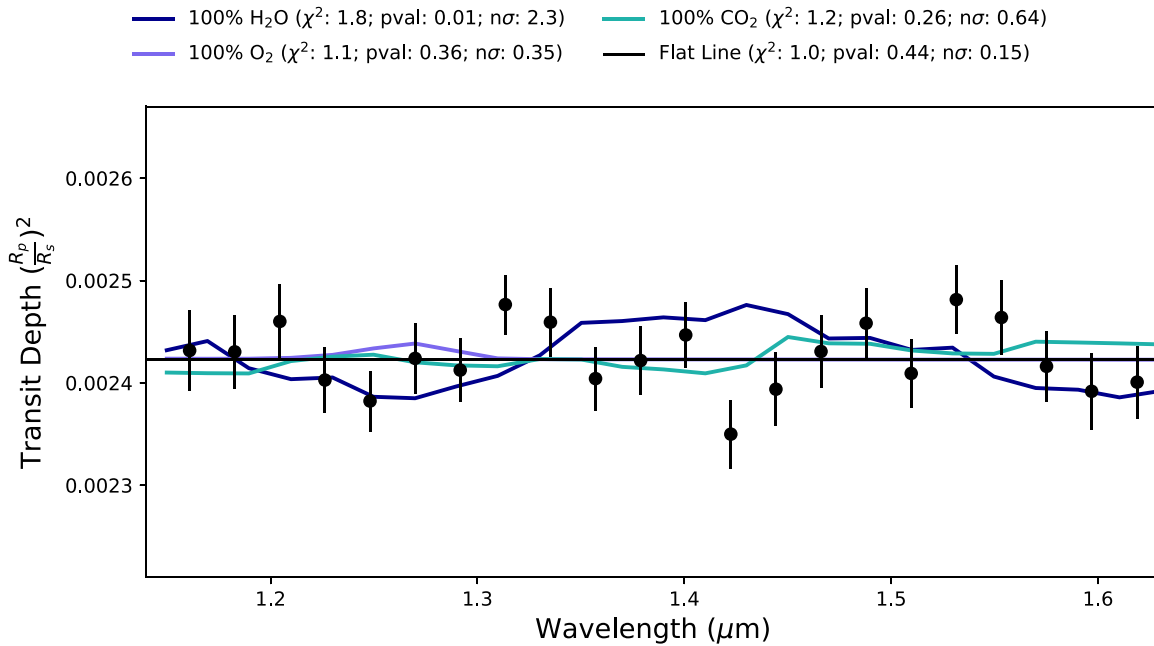


Figure 13. Same as Figure 12, except with 100% molecular composition atmospheric models for comparison. We are unable to rule out any of these atmospheric models, as their higher mean molecular weights produce transit depth variations smaller than the precision of the data points.

$>4.8\sigma$ significance. This corresponds an atmospheric mean molecular weight >8.9 amu (if an atmosphere exists). For comparison, a $1\times$ solar atmosphere has a mean molecular weight of 2.3 amu, 100% H_2O is 18 amu, O_2 is 32 amu, and CO_2 is 44 amu. From these values, an 8.9 amu could represent an atmosphere mixed with 44% H_2O and 56% H/He by volume. The higher mean molecular weight model atmospheres of $600\times$ solar and $1000\times$ solar metallicities fit the WFC3 spectrum with χ_r^2 of 2.6 (p -value of 0.0025) and 1.3 (p -value of 0.14), respectively, and cannot be confidently ruled out.

Given GJ 1132b’s equilibrium temperature of 580 K (Bonfils et al. 2018), it is more likely that this planet possesses a high mean molecular weight secondary atmosphere such as a CO_2 -dominated atmosphere similar to that of Venus, a tenuous O_2 atmosphere as discussed in Schaefer et al. (2016), or no atmosphere at all. When comparing atmospheric models of 100% H_2O , O_2 , and CO_2 with the WFC3 data, we calculated respective χ_r^2 values of 1.8 (p -value of 0.01), 1.1 (p -value of 0.34), and 1.2 (p -value of 0.26). From these statistics and as illustrated in Figure 13, we cannot rule out any of these scenarios with the current WFC3 precision. However, between GJ 1132b’s temperature, its proximity to its M-dwarf host star, and the lack of a detected hydrogen exosphere (Waalkes et al. 2019), it is unlikely that the planet retains a large H_2O -dominated atmosphere.

4.2.2. Models with Clouds and Hazes

Featureless exoplanet transmission spectra can be attributed to two different causes: a higher mean molecular weight atmosphere (and thus smaller scale height) or a high-altitude aerosol layer muting or blocking absorption features. While GJ 1132b’s temperature and terrestrial nature suggest a high mean molecular weight atmosphere, the WFC3 observations alone cannot rule out the possibility of a H/He-dominated atmosphere combined with condensate clouds such as ZnS or KCl (Morley et al. 2013) or organic photochemical hazes. We

therefore determine the altitude required for an aerosol layer on top of a low mean molecular weight atmosphere to mute all features in the WFC3 transmission spectrum. Assuming a $1\times$ solar composition, we placed aerosol layers at increasing altitudes until we obtained a spectrum that agrees with the data (p -value of 0.001; process described in detail in Libby-Roberts et al. 2020). We found that this layer must lie at pressure levels <0.4 mbars in order to mute the features of a H/He-dominated atmosphere. For comparison, Kreidberg et al. (2014) determine the cloud layer on the sub-Neptune GJ 1214b lies at pressure levels <0.01 mbars, assuming a low mean molecular weight atmosphere.

We further tested the possible existence of an aerosol layer above a $1\times$ solar atmosphere by performing a back-of-the-envelope calculation as to whether GJ 1132b could maintain a H/He primordial envelope over its lifetime. Owen et al. (2020) show that low-mass planets similar to GJ 1132b can accrete around 1% of their masses in H/He gas during formation. With a current mass of $1.66 M_\oplus$, this would translate to a starting H/He envelope mass of $0.0166 M_\oplus$. Waalkes et al. (2019) approximated a neutral hydrogen mass-loss rate of $0.86 \times 10^9 \text{ g s}^{-1}$. Assuming no secondary sources of hydrogen and a constant mass-loss rate, GJ 1132b would lose such an atmosphere in 3.7 Gyr. Berta-Thompson et al. (2015) approximate this system to be >5 Gyr, derived from the slow stellar rotation and lack of significant stellar activity. The stellar flux from GJ 1132 would have been higher in the past, thus the present-day mass-loss rate is a lower limit for GJ 1132b. Therefore, it is unlikely that GJ 1132b could maintain a present-day cloudy primordial H/He-dominated atmosphere with a $1\times$ solar composition unless there was some means of continually replenishing the escaping hydrogen and helium atoms. That said, uncertainties on the mass-loss rate, stellar flux output over the GJ 1132’s lifetime, and even the age of the system would change this calculation by several orders of magnitude. Further rigorous analysis and/or future higher-precision observations are required to completely rule out the

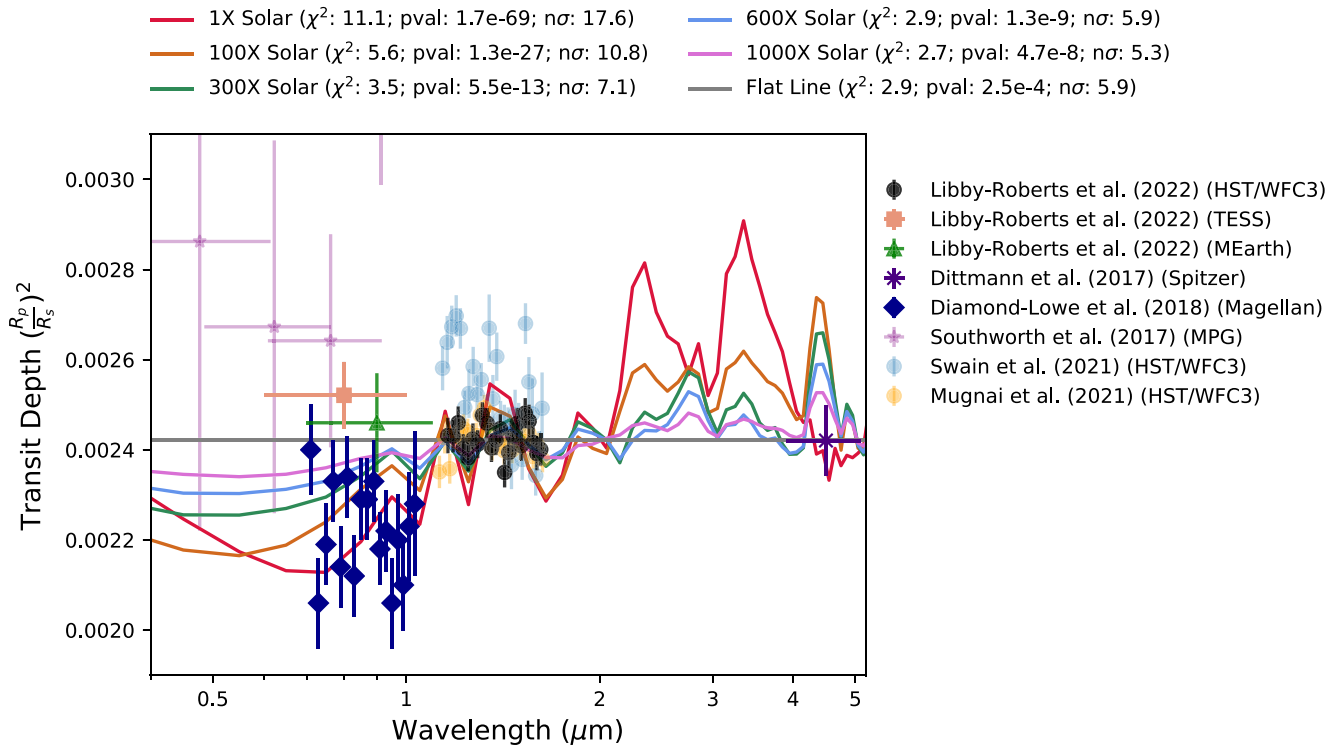


Figure 14. The 0.7–4.5 μm transmission spectrum of GJ 1132b, combining all available archival data sets with as-published transit depths. The same atmospheric models from Figure 12 are included for comparison. Goodness-of-fit values for each model were calculated using the LDSS3C spectrum, TESS, MEarth, and Spitzer photometry, and the WFC3 depths from this work. The noisy z-band flux point (Southworth et al. 2017) was cropped out to ease model visualization on the y-axis. From the χ_r^2 calculated with as-published depths, it appears that no planetary atmosphere model explains all transit depths; however, this is largely driven by the disagreement in the optical LDSS3C spectroscopic depths.

hypothesis of a cloudy low mean molecular weight atmosphere around GJ 1132b.

4.2.3. GJ 1132b’s Atmospheric Composition Determined from Archival Data

A direct comparison between all archival data to the various models shows that every atmospheric model (featureless or otherwise) is ruled out with $>5\sigma$ confidence (Figure 14). This is largely driven by the offset of the Diamond-Lowe et al. (2018) spectroscopic points in the optical compared with the other archival transit depths—including the broadband points from TESS and MEarth, which span similar wavelengths. Given the discrepancy between the spectroscopic and broadband LDSS3C transit depths, we must treat the relative changes in the transit depths within the spectrum as accurate, but not as the absolute depth. We fit for then apply a vertical offset to the Diamond-Lowe et al. (2018) points such that they best fit each of the different atmospheric models along with the TESS, MEarth, and Spitzer broadband points and our WFC3 spectrum. Each model has a different corresponding offset associated with it: -15.9 ppm ($1\times$ solar), 112.3 ppm ($100\times$ solar), 149.5 ppm ($300\times$ solar), 170.1 ppm ($600\times$ solar), 181.6 ppm ($1000\times$ solar), and 205.7 ppm (flat line). Statistics comparing the models to the WFC3 and archival data are calculated using the respective vertical offset derived from the respective model. We plot examples of these offsets in Figure 15 and 16 with the best-fit offsets for a flat line and for a $1\times$ solar metallicity applied to the Diamond-Lowe et al. (2018) points, respectively. However, the statistics listed in these plots and in this section are calculated assuming the

corresponding offset assigned to each respective model. From this, we find the addition of literature data across 0.7 – 4.5 μm enables us to rule out $1\times$, $100\times$, and $300\times$ solar metallicities by volume with respective confidences of 17.6σ , 10.3σ , and 5.6σ . A flat line remains the best-fit model with a χ_r^2 of 1.01 (p -value: 0.45), while $600\times$ and $1000\times$ solar metallicity models have χ_r^2 of 2.0 (p -value: 0.00035) and 1.5 (p -value: 0.033), respectively. Notably, the Spitzer 4.5 μm point disagrees with the $600\times$ solar metallicity model with $>2\sigma$. However, it remains the only observation at wavelengths longer than the 1.63 μm cutoff from the WFC3 spectrum. Future JWST observations will be able to fill in this wavelength gap with a precise spectrum.

5. Starspot Contamination

Spatial inhomogeneities on the surface of a star can influence planetary transit depths in a wavelength-dependent fashion, potentially mimicking the signal of absorption through a planetary atmosphere. A planet transiting across a dark spot or a bright facula can show a wavelength-dependent bump (Pont et al. 2008; Espinoza et al. 2019) that could modify transit depths if not identified and corrected. More perniciously, even a planet transiting an unspotted patch of photosphere will be blocking starlight that is unrepresentative of the average for the star as a whole. This introduces features in observed transit depths (and transmission spectrum) that express the difference between the spotted and unspotted surface (Czesla et al. 2009; Sing et al. 2011). Termed the “transit light source effect” (TLSE) by Rackham et al. (2018), this unocculted starspot phenomenon poses a particular challenge for infrared

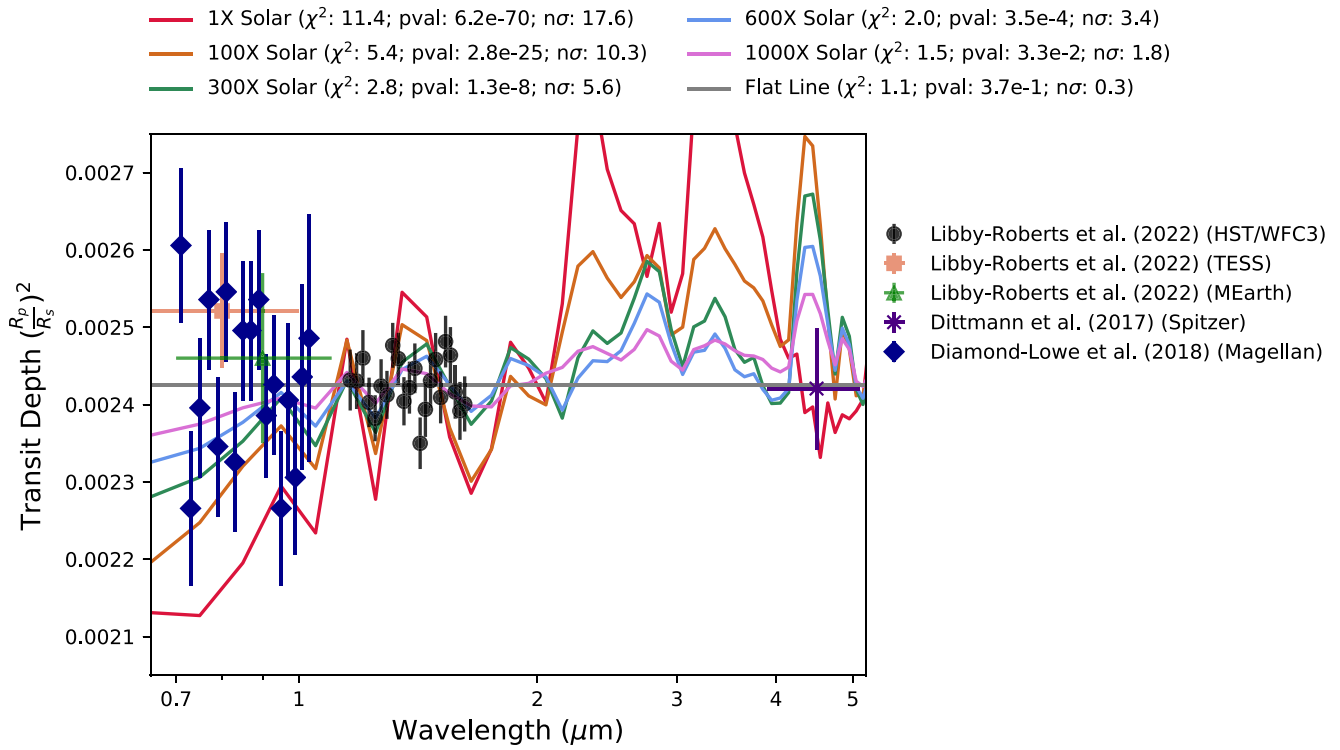


Figure 15. Similar to Figure 14, but including the best-fit flat line offset of 205.7 ppm added to the Diamond-Lowe et al. (2018) spectroscopic transit depths for visualization. Best-fit statistics noted above the plot are calculated by applying the best-fit offset to the Diamond-Lowe et al. (2018) points for their respective models. The addition of archival data strongly supports a featureless transmission spectrum from 0.7 to 4.5 μm for GJ 1132b.

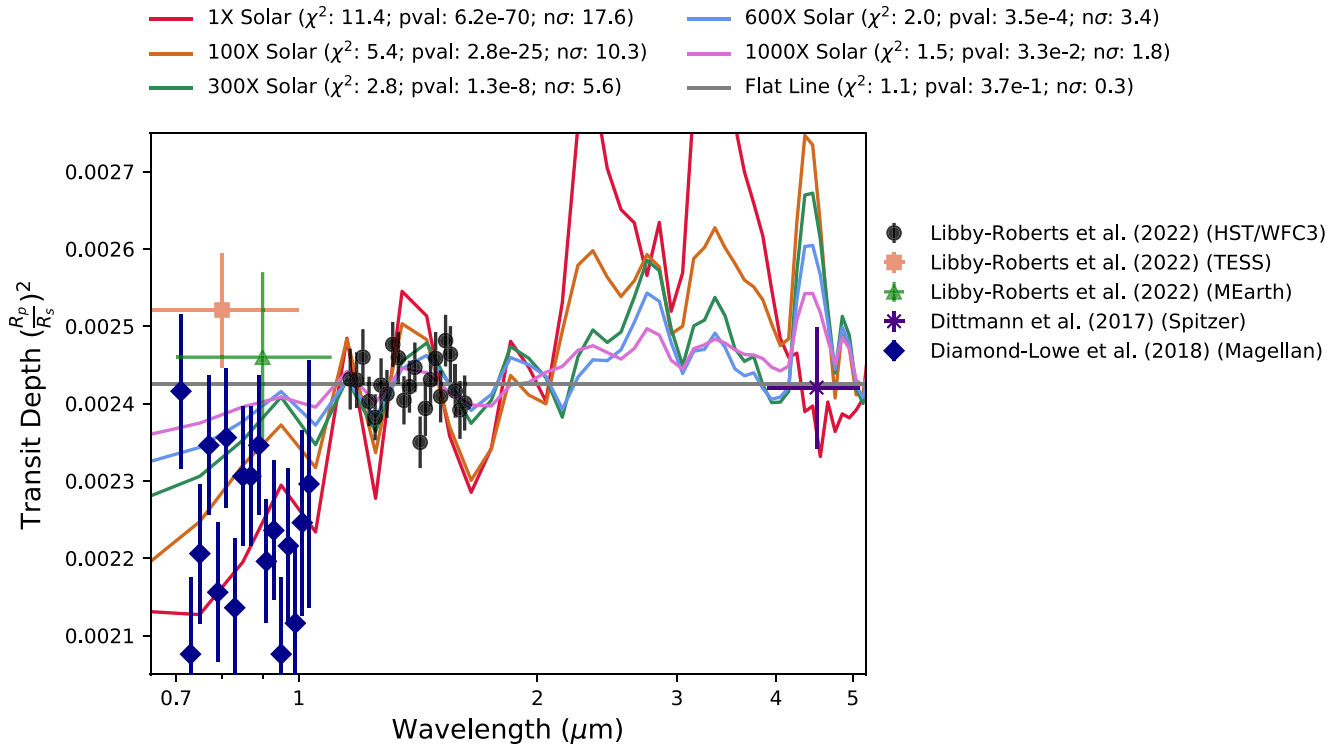


Figure 16. Similar to Figure 15, including the best-fit $1\times$ solar metallicity model offset of 15.9 ppm added to the Diamond-Lowe et al. (2018) spectroscopic transit depths for visualization.

observations of planets transiting cool stellar hosts. M dwarfs have strong molecular features in their photospheres that vary in and out of spots, meaning they can introduce spurious transit depth features from molecules like water that might also be

expected in a planet’s transmission spectrum (see also Zhang et al. 2018; Wakeford et al. 2019).

Although this work does not detect significant features in GJ 1132b’s transmission spectrum, we nonetheless model the

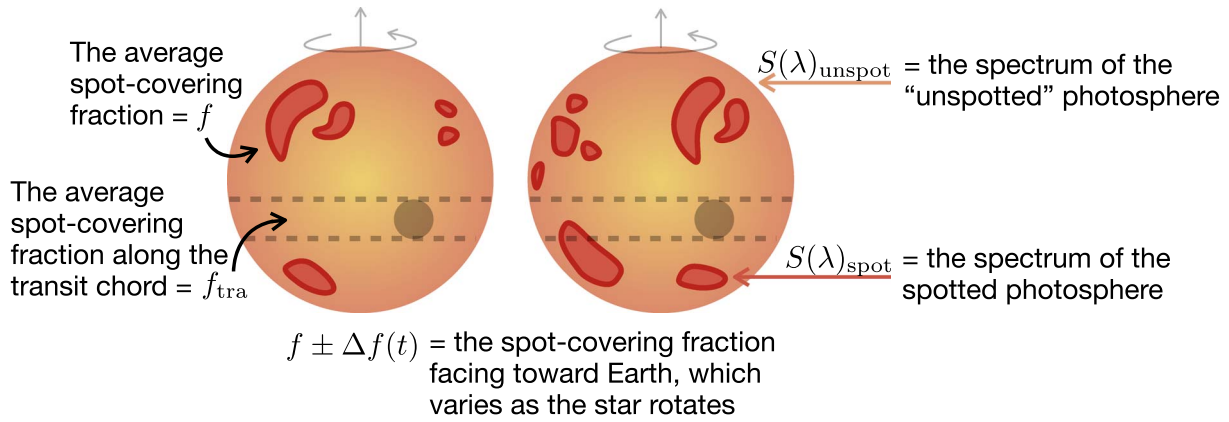


Figure 17. Definition of the variables used for modeling the impact of stellar surface inhomogeneities on the inferred transmission spectrum. In this framework, “spots” can represent patches that are either cooler or hotter than the surrounding stellar photosphere.

TLSE for this system with two goals in mind. First, the WFC3 transit depths are sufficiently precise that the lack of an observed TLSE can tell us something useful about possible spot configurations for the star—and allow us to quantify the influence spots may have on future observations at other wavelengths. Second, by explicitly modeling the TLSE, we can assess and rule out the possibility that an unfortunate arrangement of hot or cold spots might introduce a spurious transit depth signal exactly opposite to genuine transmission spectrum features and thereby mask real planetary absorption. Results from this analysis may be useful both to our understanding of the heterogeneous photospheres of low-mass M dwarfs and to future planned observations of GJ 1132b.

5.1. Starspot Model

The wavelength-dependent transit depth of a planet transiting a spotless star can be written as $D(\lambda) = (R_p/R_s)^2 + \Delta D(\lambda)_{\text{atm}}$, where the first term represents the transit depth of the planet at a reference radius (such as a rocky surface or a one-bar level in its atmosphere) and $\Delta D(\lambda)_{\text{atm}} = 2HR_p/R_s^2 \times n(\lambda)$ represents the absorption by the planet’s atmosphere making the planet appear larger by $n(\lambda)$ scale heights at different wavelengths. In this section, we instead aim to model $D(\lambda)$ as an atmosphere-less planet transiting a spotted star. We rewrite the wavelength-dependent depth as $D(\lambda) = (R_p/R_s)^2 + \Delta D(\lambda)_{\text{spot}}$, where the spot-induced depth variations ($\Delta D(\lambda)_{\text{spot}}$) can be either positive or negative. Approximately following the derivations outlined in Rackham et al. (2018) and Zhang et al. (2018), the spot-induced depth variation can be estimated as

$$\Delta D(\lambda)_{\text{spot}} = \left(\frac{R_p}{R_s}\right)^2 \times \left[\frac{(1 - f_{\text{tra}}) + f_{\text{tra}} \frac{S(\lambda)_{\text{spot}}}{S(\lambda)_{\text{unspot}}}}{(1 - f) + f \frac{S(\lambda)_{\text{spot}}}{S(\lambda)_{\text{unspot}}}} - 1 \right], \quad (2)$$

with effectively three unknowns: the flux ratio $S(\lambda)_{\text{spot}}/S(\lambda)_{\text{unspot}}$, the global spot covering fraction f , and the transit-chord spot covering fraction f_{tra} , which are summarized in Figure 17 and below.

1. The spectral fluxes $S(\lambda)_{\text{spot}}$ and $S(\lambda)_{\text{unspot}}$ of the spotted and unspotted photospheres, respectively, represent the flux (in $\text{W}/\text{m}^2/\text{nm}$ or related units) emitted by two different types of stellar photosphere. For this work, we

use solar-metallicity model stellar spectra from Husser et al. (2013)¹⁵ for a surface gravity of $\log g = 5.0$, which closely matches that of GJ 1132, so the temperature (T_{spot} or T_{unspot}) uniquely determines the spectrum. To maintain generality for modeling spots or faculae, T_{spot} is allowed to be either cooler or warmer than T_{unspot} . By using fluxes instead of angle-dependent intensities, we are ignoring the effects of limb darkening but still sensitive to the effect of starspots averaged over the entire stellar disk.

2. The average spot covering fraction f represents the long-term average of the fraction of the Earth-facing stellar disk covered with spots. The instantaneous spot covering fraction facing Earth at any particular time t can be written as $f \pm \Delta f(t)$, where $\Delta f(t)$ represents the variability due to rotation (or, potentially, spot evolution). For example, a star with an average spot covering fraction of $f = 20\%$ might exhibit an Earth-facing spot covering fraction ranging from 19% to 21% as it rotates through one or more periods. $\Delta f(t)$ therefore has a semi-amplitude of 1%. It is important to separate the time-variable term from the average spot covering fraction, as the TLSE depends on the total spot covering fraction in and out of the transit chord, not just the (always smaller) fraction producing out-of-transit modulations. The model for $\Delta D(\lambda)_{\text{spot}}$ described here represents the time-averaged impact of starspots on the transit depth rather than the variability from epoch to epoch. This effectively assumes that transits will be observed over multiple epochs and/or that the static signal will dominate over the time-variable contribution to the transit depth.
3. The transit chord spot covering fraction f_{tra} represents a similar time average along the narrow slice of the stellar disk transited by the planet; the amplitude of $\Delta D(\lambda)_{\text{spot}}$ depends on the difference in the spot covering fraction between the disk and the surface actually blocked by the planet. For this work, we assume that $f_{\text{tra}} = 0$. Motivated by the lack of obvious spot-crossing features observed in transits, this assumption considerably simplifies Equation 2. However, the f we infer through modeling will more accurately represent how spotted the average disk surface is *relative* to the transit chord. It is effectively assuming that the stellar flux along the transit chord can

¹⁵ Available for download at <https://phoenix.astro.physik.uni-goettingen.de/>

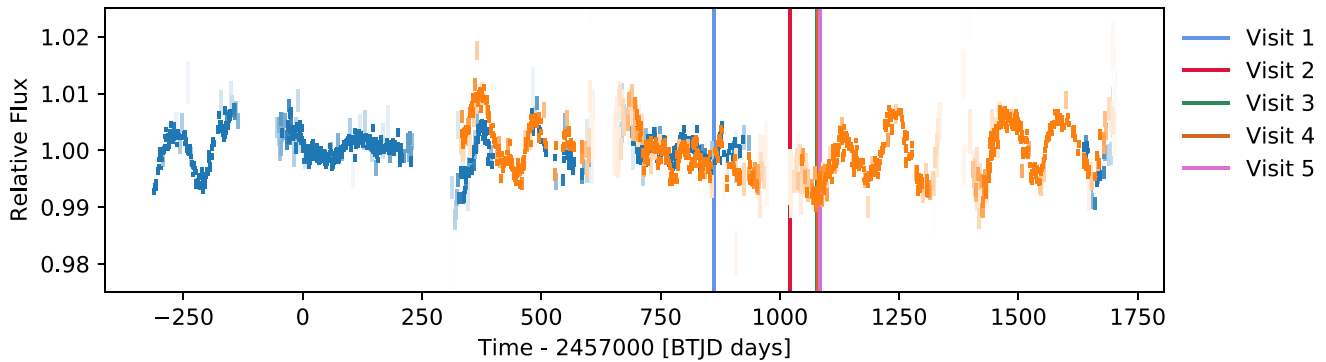


Figure 18. MEarth out-of-transit light curve of GJ 1132, in the MEarth photometric bandpass (roughly 715–1000 nm), corrected for time-variable precipitable water vapor in Earth’s atmosphere. Nightly bins are shown with a color intensity inversely proportional to the nightly variance, for two MEarth telescopes (t_{e113} in blue, t_{e116} in orange). The epochs of the five WFC3 visits are marked with vertical lines.

be well-represented by a single-temperature PHOENIX atmosphere; the rest of the stellar disk comprises a f -weighted average of spectra at two different temperatures.

5.2. Starspot Data and Priors

To connect this conceptual framework directly to the specific case of GJ 1132b transiting its mid-to-late M dwarf, we apply three data constraints and three priors.

Data Constraint (1) = The semi-amplitude of out-of-transit modulations—In this model, as a star rotates, the time-variable integrated stellar flux $S(\lambda) + \Delta S(\lambda, t)$ should change with time according to

$$\frac{\Delta S(\lambda, t)}{S(\lambda)} = -\Delta f(t) \left[\frac{1 - \frac{S(\lambda)_{\text{spot}}}{S(\lambda)_{\text{unspot}}}}{1 - f \left(1 - \frac{S(\lambda)_{\text{spot}}}{S(\lambda)_{\text{unspot}}} \right)} \right], \quad (3)$$

which when integrated over any particular bandpass can be compared directly to the semi-amplitude of observed photometric modulations. The star GJ 1132 has been monitored nearly continuously by the MEarth Observatory (Newton et al. 2018) since before the discovery of GJ 1132b. These data trace the photometric variability $\Delta S(\lambda, t)/S(\lambda)$ of the star due to rotation or starspot evolution, integrated over the MEarth RG715 filter bandpass (roughly 700–1000 nm). MEarth out-of-transit monitoring data for GJ 1132, spanning February 2014 through 2019 August, are shown in Figure 18.¹⁶ For the data shown here, all high-cadence transit follow-up observations were excluded. Time-variable precipitable water vapor can introduce long-term wobbles to M dwarfs’ light curves observed with MEarth, because telluric water absorbs more light from these red stars than their typically much bluer comparisons. We correct for this effect by binning together all M dwarf light curves from a site to derive a “common mode” light curve that traces the effects of changing water vapor. To approximately correct for water vapor variations, we fit for the multiplicative factor that best scales this common mode to match the GJ 1132 light curve, and we then subtract the resulting scaled time series (see Berta et al. 2012; Newton et al. 2016). Some residual trends are not perfectly corrected through

this process, as seen by the disagreements where data from two MEarth telescopes overlap. From the subset of these data that were available at the time, Berta-Thompson et al. (2015) estimated a rotation period for GJ1132 of approximately 125 days, Cloutier et al. (2017) estimated 122^{+6}_-5 days, and Newton et al. (2018) estimated 130 ± 13 days. The more recent data (Figure 18) continue to support these inferences of a stellar rotation period of roughly 120–130 days. The variation in the light curve’s appearance from season to season over 5 yr of observations clearly indicates significant starspot evolution and/or differential rotation. We estimate by eye the semi-amplitude of $\Delta S(\lambda, t)/S(\lambda)$ to be about $1.0 \pm 0.2\%$ in the MEarth bandpass. Though TESS and Spitzer also provide precise out-of-transit monitoring, the data sets span durations much shorter than the star’s rotation period and therefore cannot be used to estimate the full range of rotational variability of the star. The out-of-transit spectra from this WFC3 program could be used to spectroscopically constrain $\Delta S(\lambda, t)/S(\lambda)$ at 1.1–1.7 μm , but Figure 18 shows the five WFC3 epochs do not sample the star at its full range of variability, so we exclude them from the analysis.

Data Constraint (2) = The integrated average stellar flux—In this model, the average integrated spectrum of the star is $S(\lambda) = fS(\lambda)_{\text{spot}} + (1 - f)S(\lambda)_{\text{unspot}}$, which is the weighted sum of the spotted and unspotted components. While this model prediction could be compared wavelength-by-wavelength to an absolutely calibrated stellar spectrum, we simplify it into a constraint that the bolometric flux from the star must match that implied by the effective temperature of the star, as

$$\sigma T_{\text{eff}}^4 = \int_{\lambda} S(\lambda) = f\sigma T_{\text{spot}}^4 + (1 - f)\sigma T_{\text{unspot}}^4, \quad (4)$$

with σ as the Stefan–Boltzmann constant. Without this, arbitrary combinations of spot covering fractions and temperatures could produce stars with extremely unrealistic integrated surface fluxes. For this work, we adopt $T_{\text{eff}} = 3270 \pm 140$ K (Berta-Thompson et al. 2015), implying $\sigma T_{\text{eff}}^4 = (6.5 \pm 1.1) \times 10^6$ W m^{−2} for GJ 1132.

Data Constraint (3) = The transit depths—In this model, $D(\lambda)$ can be calculated with Equation (2) and compared directly to observed transit depth at any wavelength. For this work, the main transit depths we include are the measured WFC3/G141 transit depths reported in Table 2. We also include the spectroscopic LDSS3C depth measurements from Diamond-

¹⁶ Available through MEarth Data Release 9 (DR9); <https://1web.cfa.harvard.edu/MEarth/DataDR9.html>.

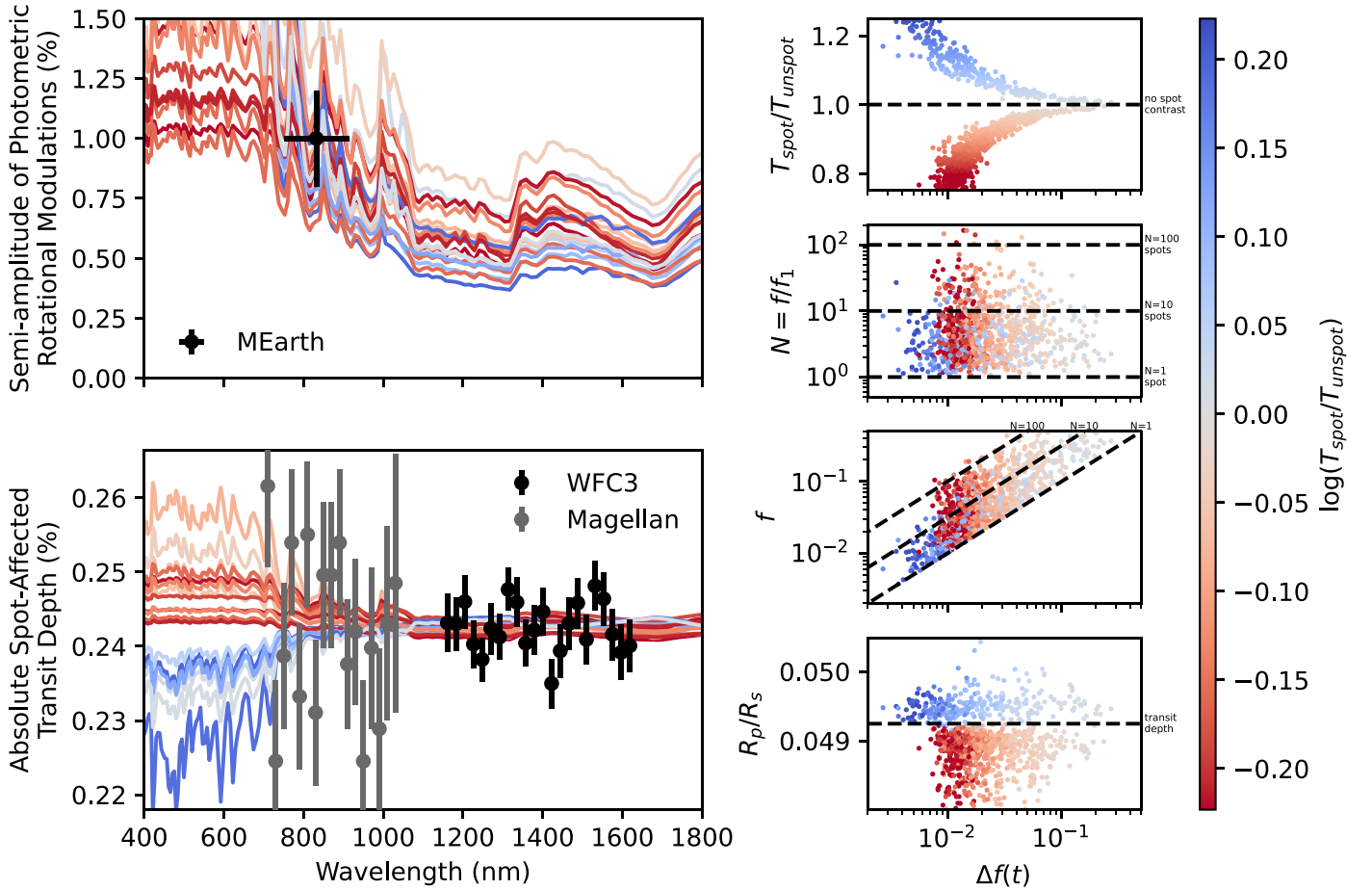


Figure 19. A visualization of the posterior probability distribution for GJ 1132’s starspot properties, including data used in the fit (*left panels*, with 20 random sample curves) and parameter samples (*right panels*, with 1000 random samples). Curves and points are colored from red to blue by $T_{\text{spot}}/T_{\text{unspot}}$, with paler colors closer to 1. Dashed lines highlight useful reference values in each parameter distribution. A fitted offset was applied to the LDSS3C depths, as explained in the text. The code used to generate this plot is available online (</>).

Lowe et al. (2018) because they are the most constraining optical measurements available. As in Section 4.1.3, we treat the absolute depth of the LDSS3C as unknown. When comparing to starspot models, we include a multiplicative offset allowing these depths to shift up and down together as a free parameter. We marginalize over this offset in all our starspot inferences. These data are shown in Figure 19, with the maximum-likelihood offset applied to the LDSS3C depths.

Prior (1) = The connection between $\Delta f(t)$ and f —In this model, the total spot covering fraction f and the variability in the Earth-facing fraction due to rotation $\Delta f(t)$ are entirely decoupled. However, through a suite of geometric simulations, Rackham et al. (2018, 2019) determined the amplitude of photometric rotational modulations generally scales as $f^{0.5}$. Such a scaling emerges naturally by treating $\Delta f(t)$ as governed by a Poisson process set by the average number of spots covering the stellar disk. If we define f_1 as the average spot covering fraction of one individual spot, the number of spots over the entire stellar disk would be $N = f/f_1$, and the expected random variation in the number of spots visible at any one time would be \sqrt{N} . This implies the expectation value for the level of rotation variability $\Delta f(t)$ should be

$$\langle |\Delta f(t)| \rangle = f_1 \sqrt{N} = \sqrt{f_1 f}. \quad (5)$$

This broadly encapsulates the behavior that high-amplitude rotation variability can emerge from either larger spots (higher f_1 at fixed f) or a more thoroughly spotted star (higher f at fixed f_1). To capture this relationship, we apply a prior that $x = [f - \Delta f(t)]/f_1 = N - \Delta f(t)/f_1$ should be drawn from a Poisson probability distribution with N as the expectation value, written as

$$P(x) = N^x e^{-N} / \Gamma(x + 1). \quad (6)$$

By using the gamma function $\Gamma(x + 1)$ instead of $x!$ in the denominator, we allow for non-integer values of the number of visible spots. Because we keep f_1 as a free parameter, this Poisson prior does not actually place new constraints on f and $\Delta f(t)$. Rather, it allows us to connect them to the typical spot size f_1 that would best explain the amplitude of rotational variability coming from random Poisson draws for the number of starspots on the Earth-facing side of the star. The inferred typical spot size hinges on the assumption that starspots are arrayed quasi-isotropically on the surface, as assumed in the calculations of Rackham et al. (2018) that showed rotational modulations scale as $f^{0.5}$. The typical spot size distribution cannot be determined robustly if spots instead congregate to densely fill active latitudes or polar caps (Guo et al. 2018).

Prior (2) = Uniform logarithmic priors on f , $\Delta f(t)$, f_1 —As the values of the spot covering fraction parameters could plausibly span orders of magnitudes, we wish for their priors to be uniform for the logarithm of the value. Therefore, we apply a logarithmic prior of the form $P(x) \propto 1/x$ on each of f , $\Delta f(t)$, and f_1 . With this prior, the probability will be uniform across logarithmic intervals, meaning the prior probability of a parameter falling in the range 10^{-3} – 10^{-2} is the same as for the range 10^{-2} – 10^{-1} . Furthermore, as the effect of covering $f > 0.5$ of the star with cool spots can be reproduced with $f < 0.5$ coverage by hot spots, we place a strict prior of $f < 0.5$ to avoid those (effectively duplicate) solutions. We also apply a prior requiring $f_1 < \Delta f(t) < f$.

Prior 3 = The range of allowable spot temperatures—In this model, spot temperatures could be arbitrarily higher or lower than the unspotted surface. However, to avoid introducing an artificial bias toward hot spots, due to the practical limitation that the PHOENIX spectra we use are not available below 2300 K, we impose a symmetrical prior that $0.75 < T_{\text{spot}}/T_{\text{eff}} < 1.25$. This range does remove some otherwise viable models, but it still includes most of the spot temperature contrast ratios inferred for cool dwarfs in the Berdyugina (2005); Fang et al. (2016), and Morris et al. (2019) starspot samples.

Together, the data constraints define a log-likelihood of $\ln L = -\frac{1}{2}\chi^2$ where $\chi^2 = \chi_{\text{modulations}}^2 + \chi_{\text{average flux}}^2 + \chi_{\text{transit depths}}^2$. The three terms follow definitions of $\chi^2 = \sum[(d_i - m_i)/\sigma_i]^2$, where d_i , m_i , and σ_i are the respective data, model, and uncertainty values for each constraint. In the case of GJ1132b, the $\chi_{\text{modulations}}^2$ sum has only one term (MEarth monitoring), the χ_{flux}^2 sum has only one term (the bolometric flux), and the $\chi_{\text{modulations}}^2$ sum includes as many terms as there are transit depth measurements (17 for LDSS3C and 22 for WFC3). We log-transform the priors described above and add them to this log-likelihood, to define the log-posterior for any set of parameters.

5.3. Starspot Inferences

We sample from the posterior distribution for the parameters T_{unspot} , T_{spot} , f , $\Delta f(t)$, f_1 , and R_p/R_s (as well as a nuisance offset for the LDSS3C depths). We use the `emcee` (Foreman-Mackey et al. 2013) ensemble sampler with 100 walkers. We sample for a total of 20,000 steps and exclude the first 10,000 steps as burn-in. Visual inspection showed that parameter distributions already appear converged by 1000 steps. The autocorrelation lengths of parameters in the flattened chain were 400–2000 steps, meaning they contained 500–2500 effectively independent samples of the posterior.

For a first experiment, we assume GJ 1132b’s atmosphere has such a high mean molecular weight that its transmission spectrum can be entirely neglected. Thus, the planet’s radius is effectively constant across wavelength and all transit depth variations are due to the effect of unocculted starspots. Figure 19 visualizes the resulting constraints on GJ 1132’s starspot properties. We plot the combinations of fitted parameters that most clearly explain phenomena in the model, and color each sample by the value of its starspot temperature ratio $T_{\text{spot}}/T_{\text{unspot}}$ so that hotter and colder spots can be traced throughout. We summarize some key conclusions from Figure 19 and this analysis as follows.

1. The data for GJ 1132 can be closely matched by the starspot model outlined above. At the peak of the posterior distribution, the data yield $\chi^2 = 46.4$ for 41 data points (one MEarth semi-amplitude, one effective temperature, and 17 LDSS3C and 22 WFC3 depths) and seven free parameters.
2. The existing data are insufficient to distinguish whether GJ 1132’s most important unocculted surface features (either spots of faculae/plage) are cooler or warmer than the surrounding photosphere. More precise optical data, more reliable knowledge of the absolute depths offset between LDSS3C and WFC3, and/or precise spectroscopic measurements of the rotational modulation semi-amplitude could distinguish between cold or hot spots.
3. The distribution of $\Delta f(t)$ and $T_{\text{spot}}/T_{\text{unspot}}$ is shaped by the need to match the semi-amplitude of the rotational modulations; MEarth’s observed 1% variability can be matched either with stronger spot contrasts or more dramatic variations in the spot covering fraction. Only hot spots can extend to $\Delta f(t) < 1\%$ and still match the 1% photometric variability, because only they can produce spot flux contrasts $> 100\%$, whereas the most that a completely dark cold spot could change a region’s surface flux by would be 100%.
4. The distribution of $\Delta f(t)$ and f is shaped additionally by the flat transit depths. f would otherwise uniformly fill the upper left triangle above $f = \Delta f(t)$, but the lack of observed spectral features in the transit depths rules out models with low variability $\Delta f(t)$ (which also have strong temperature contrast) and high average covering fraction f .
5. The average number of visible spots $N = f/f_1$ is mostly < 10 , as shown by dashed lines plotted on the distributions for f and N . Models with large numbers of very small spots would require values of f that would be too high for a given $\Delta f(t)$ and thus introduce strong spectral features into the transit depths. The values of $f = 0.044_{-0.027}^{+0.094}$ are generally $2 - 3 \times$ the values of $\Delta f(t) = 0.018_{-0.008}^{+0.029}$. The typical single-spot covering fraction $f_1 = 0.010_{-0.006}^{+0.016}$; as a fraction of the 2π steradians of the Earth-facing side of the star, this would correspond to typical spot radii of $1.1_{-0.8}^{+1.3}$ degrees. These sizes are about $2 \times$ larger than the Sun’s largest spots at solar maximum (Mandal et al. 2017) and similar to the largest active regions recorded on the Sun (Hoge 1947; Nicholson 1948). If the planet transited one of these spots at disk center, the crossing event would last about a minute and likely fall entirely within a single WFC3 exposure. We did observe a few single-point outliers in the broadband transit light curves (Figure 3), but as there were also outliers in the out-of-transit baseline, we cannot uniquely attribute them to starspot crossing events.
6. The true planet-to-star radius ratio R_p/R_s changes depending on whether the unocculted spots are cold or hot. If the spots are cold, the transit chord is brighter than the rest of the star, so the transit depth overestimates R_p/R_s (and vice versa). Marginalizing over both cold and hot spots, we find the true $R_p/R_s = 0.0490_{-0.0003}^{+0.0005}$. For GJ 1132b, the flat transit spectrum constrains the spot-induced uncertainties on R_p/R_s to be broadly similar to the statistical uncertainties on this quantity—and negligible compared to the uncertainties on the stellar radius.

The above conclusions connecting rotational variability to the average spot covering fraction rely on an assumption that the longitudinal distribution of spots is random and isotropic. This could be broken by, for example, a large polar spot or an extremely dense zonal band. Such extreme symmetries would exhibit little photometric variability but imbue conspicuous spectral features into the WFC3 depths. We see the opposite (strong photometric variability and flat WFC3 depths), suggesting the Poisson-based approach used here may be valid.

For an additional experiment, we ask whether an unfortunate arrangement of starspots could artificially erase the transmission spectrum of a H/He-rich atmosphere by producing a starspot signal that exactly cancels the transit depths from the planet’s atmosphere. To answer this question, we attempted to model the observed flat transit depths with a superposition of the starspot model with a $100\times$ solar metallicity atmosphere for the planet. In contrast to the fit shown in Figure 19, where the planet’s transmission spectrum was assumed to be flat, this exercise tests whether starspot parameters can be found that would be able to completely erase the transit depth signal of a large-amplitude H/He-rich planet atmosphere.

We repeat the sampling procedure as above, but for simplicity exclude the LDSS3C depths. The result of this fit is that hot spots with strong temperature contrasts and large covering fractions can produce inverted water features that qualitatively mimic those needed to mask the planet’s transmission spectrum (as also seen in TRAPPIST-1, Zhang et al. 2018). However, at the peak of the posterior, $\chi^2 = 59.2$ for 24 data points (one MEarth semi-amplitude, one effective temperature, and 22 WFC3 depths) and six free parameters. This is a poor match to the data (p -value of 3×10^{-6}), mostly driven by the mismatch in shape between the cool water features in the transmission model and the hot water features in the stellar spectra. Based on this test, we disfavor a scenario where GJ 1132b has a clear H/He-dominated atmosphere that happens to be masked by starspot contamination.

Another related way of partially canceling out strong transmission features is the spectral resolution-linked bias (Deming & Sheppard 2017). Transit depths observed at low spectral resolution will be biased toward wavelengths where the star is brightest within each bin. If strong planetary absorption features align in wavelength with deep stellar absorption features, as water lines would do for GJ 1132b and GJ 1132, transmission features will be suppressed. Deming & Sheppard (2017) show the feature suppression to be at the level 12% for TRAPPIST-1 (500 K cooler than GJ 1132) at WFC3 wavelengths; we do not account for this effect anywhere in our analyses.

Currently available data suggest that unocculted starspots affect GJ 1132b’s transit depths at about the 100 ppm level in the optical and about the 10 ppm level for wavelengths longer than $1 \mu\text{m}$. Starspots do not pose a serious problem for the HST/WFC3 transmission spectrum of this target, but future analyses of transit observations with JWST or other large telescopes should be aware of the potential contaminating influence of the star’s mottled surface.

6. Conclusion

We investigated the HST/WFC3 transmission spectrum of GJ 1132b, a rocky super-Earth orbiting a nearby bright M dwarf, over five separate visits. We determined a featureless spectrum to a precision of 34 ppm in 20 nm wavelength bins

spanning $1.15\text{--}1.63 \mu\text{m}$. From this result, we rule out the presence of a cloud-free H/He-dominated atmosphere with a mean molecular weight less than 8.9 amu at 4.8σ confidence. High-altitude aerosol layers at pressures less than 0.4 mbars could potentially flatten the features of a solar composition atmosphere. Using the predicted mass-loss rate estimated by Waalkes et al. (2019), we find that a primordial H/He atmosphere composing 1% of GJ 1132b’s mass could be removed in 3.7 Gyr by the current high-energy irradiation from the star GJ 1132. With an age >5 Gyr and the much more intense radiation environment it experienced in the past, GJ 1132b is unlikely to possess any primordial H/He-dominated atmosphere. We therefore conclude that the most likely scenario for GJ 1132b is that it has a high-metallicity secondary atmosphere, like Venus’s CO_2 -dominated atmosphere, the eroded O_2 -dominated atmospheres predicted by Schaefer et al. (2016), or no atmosphere at all. Current data cannot speak to the total mass in such a secondary atmosphere, which could range from a Venusian-like thick atmosphere to Mercurial-like tenuous exosphere. This conclusion is contrary to the recent work by Swain et al. (2021), who use a different analysis of the same data set to infer an H/He-rich atmosphere with a Rayleigh scattering slope and HCN and CH_4 absorption. Our results are consistent with the featureless spectrum found by Mugnai et al. (2021).

We analyzed the GJ 1132 TESS light curve and determined a broadband transit depth and orbital parameters for GJ 1132b consistent with those from the WFC3 transits and previous Spitzer measurements in Dittmann et al. (2017). A search for GJ 1132c transits in the TESS data was unsuccessful, yielding a 3σ upper limit of $1.84 R_{\oplus}$ on the radius of the planet if it transits. Indeed, if GJ 1132c were completely co-planar with GJ 1132b, it would not transit. Instead, GJ 1132c requires an orbital inclination of 89.88° (1.2° difference from GJ 1132b) or more for a transit to occur along our line of sight. Bonfils et al. (2018) note that there is a less than 1% chance this planet transits, supporting our nondetection in the TESS light curve.

Combining our GJ 1132b WFC3 spectrum with the TESS broadband depth, our updated MEarth depth, and other archival GJ 1132b transit depths (Dittmann et al. 2017; Diamond-Lowe et al. 2018) yielded a transmission spectrum covering $0.7\text{--}4.5 \mu\text{m}$ for this planet. We determined that the spectroscopic transit depths from Diamond-Lowe et al. (2018) demonstrate a significant offset from the other data sets, due to possible instrumental effects. Fitting an offset to the Diamond-Lowe et al. (2018) points, we find that the majority of data sets (besides Southworth et al. 2017; Swain et al. 2021) rule out $<300\times$ solar metallicity by volume atmospheric compositions with $>5.6\sigma$ confidence. The best-fit model across all points remained a featureless flat line with a χ_r^2 of 1.01 (p -value: 0.45). Future JWST observations or ground-based observations from the upcoming ELTs will be helpful in discerning the existence of an atmosphere around GJ 1132b, and if one exists, determining its composition.

We explored the influence of unocculted spots on the measured transit depths to assess whether they are able to corrupt the transmission spectrum we infer for the planet. We used a flexible definition for spots as surface features that could be either cool (dark patches of magnetically-suppressed convection) or hot (bright patches like faculae or plage). Given all available data and a Poisson-based model for rotational variability, we estimated that the total spot covering fraction on







GJ 1132 is typically $2\text{--}3\times$ larger than the asymmetric distribution of spots that rotates in and out of view and that spot features have typical radii of $0.2^\circ\text{--}2^\circ$. We find the likely effect of starspots on GJ 1132b's transit depths to be about 100 ppm in the optical and about 10 ppm in the infrared. As these are comparable to the amplitude of features expected from a secondary atmosphere, future observational studies of GJ 1132b's transmission spectrum should carefully account for unocculted spots.

We would like to acknowledge the anonymous referee for providing helpful insights and suggestions regarding this work. We thank our Program Coordinator Tricia Royle and Contact Scientist Peter McCullough for their efforts to optimize and schedule the WFC3 observations, as well as the entire team that makes Hubble the telescope that it is. We also thank Will Waalkes, Girish Duvvuri, and Carlos Cruz-Arce for their helpful conversations and suggestions on this project. We gratefully acknowledge that this work is based on observations made with the NASA/ESA Hubble Space Telescope, obtained from the data archive at the Space Telescope Science Institute (STScI) and supported by NASA through grant numbers HST-GO-14758 and HST-AR-15788 from STScI. STScI is operated by the Association of Universities for Research in Astronomy, Inc. under NASA contract NAS 5-26555. This material is also based upon work supported by NASA under grant No. 80NSSC18K0476 issued through the XRP Program. This publication was made possible through the support of a grant from the John Templeton Foundation. The opinions expressed here are those of the authors and do not necessarily reflect the views of the John Templeton Foundation. Z.K.B.-T. is thankful for support from the National Science Foundation NSF/CAREER program under grant 1945633. B.V.R. thanks the Heising-Simons Foundation for support. J.M.D. acknowledges support from the Amsterdam Academic Alliance (AAA) Program, and the European Research Council (ERC) European Union's Horizon 2020 research and innovation program (grant agreement No. 679633; Exo-Atmos). This work is part of the research program VIDI New Frontiers in Exoplanetary Climatology, with project number 614.001.601, which is (partly) financed by the Dutch Research Council (NWO).






Facilities: HST(WFC3), TESS, MEarth.

Software: Astropy (Astropy Collaboration et al. 2013, 2018), Photutils (Bradley et al. 2019), emcee (Foreman-Mackey et al. 2013), BATMAN (Kreidberg 2015), LDTK (Parviainen & Aigrain 2015), Iraclis (Tsiaras et al. 2016a, 2016b), RECTE (Zhou et al. 2017), Exo-Transmit (Kempton et al. 2017), Lightkurve (Lightkurve Collaboratio et al. 2018).

ORCID iDs

Jessica E. Libby-Roberts  <https://orcid.org/0000-0002-2990-7613>
 Zachory K. Berta-Thompson  <https://orcid.org/0000-0002-3321-4924>
 Hannah Diamond-Lowe  <https://orcid.org/0000-0001-8274-6639>
 Michael A. Gully-Santiago  <https://orcid.org/0000-0002-4020-3457>
 Eliza M.-R. Kempton  <https://orcid.org/0000-0002-1337-9051>
 Benjamin V. Rackham  <https://orcid.org/0000-0002-3627-1676>

David Charbonneau  <https://orcid.org/0000-0002-9003-484X>

Jean-Michel Désert  <https://orcid.org/0000-0002-0875-8401>
 Jason A. Dittmann  <https://orcid.org/0000-0001-7730-2240>
 Ryan Hofmann  <https://orcid.org/0000-0002-5556-6840>
 Caroline V. Morley  <https://orcid.org/0000-0002-4404-0456>
 Elisabeth R. Newton  <https://orcid.org/0000-0003-4150-841X>

References

- Astropy Collaboration, Robitaille, T. P., Tollerud, E. J., et al. 2013, *A&A*, **558**, A33
 Astropy Collaboration, Price-Whelan, A. M., Sipőcz, B. M., et al. 2018, *AJ*, **156**, 123
 Berdyugina, S. V. 2005, *LRSP*, **2**, 8
 Berta, Z. K., Irwin, J., Charbonneau, D., Burke, C. J., & Falco, E. E. 2012, *AJ*, **144**, 145
 Berta, Z. K., Charbonneau, D., Désert, J.-M., et al. 2012, *ApJ*, **747**, 35
 Berta-Thompson, Z. K., Irwin, J., Charbonneau, D., et al. 2015, *Natur*, **527**, 204
 Bonfils, X., Almenara, J. M., Cloutier, R., et al. 2018, *A&A*, **618**, A142
 Bradley, L., Sipocz, B., Robitaille, T., et al. 2019, astropy/photutils: v0.6, Zenodo, doi:10.5281/zenodo.2533376
 Claret, A., Hauschildt, P. H., & Witte, S. 2012, *A&A*, **546**, A14
 Cloutier, R., Doyon, R., Menou, K., et al. 2017, *AJ*, **153**, 9
 Czesla, S., Huber, K. F., Wolter, U., Schröter, S., & Schmitt, J. H. M. M. 2009, *A&A*, **505**, 1277
 Deming, D., & Sheppard, K. 2017, *ApJL*, **841**, L3
 Deming, D., Wilkins, A., McCullough, P., et al. 2013, *ApJ*, **774**, 95
 Diamond-Lowe, H., Berta-Thompson, Z., Charbonneau, D., & Kempton, E. M. R. 2018, *AJ*, **156**, 42
 Diamond-Lowe, H., Youngblood, A., Charbonneau, D., et al. 2021, *AJ*, **162**, 10
 Dittmann, J. A., Irwin, J. M., Charbonneau, D., Berta-Thompson, Z. K., & Newton, E. R. 2017, *AJ*, **154**, 142
 Eastman, J., Siverd, R., & Gaudi, B. S. 2010, *PASP*, **122**, 935
 Encrenaz, T., & Coustenis, A. 2018, in *Handbook of Exoplanets*, ed. H. J. Deeg & J. A. Belmonte (Cham: Springer), 45
 Espinoza, N., Rackham, B. V., Jordán, A., et al. 2019, *MNRAS*, **482**, 2065
 Fang, X.-S., Zhao, G., Zhao, J.-K., Chen, Y.-Q., & Bharat Kumar, Y. 2016, *MNRAS*, **463**, 2494
 Foreman-Mackey, D., Hogg, D. W., Lang, D., & Goodman, J. 2013, *PASP*, **125**, 306
 Forget, F., & Leconte, J. 2014, *RSPTA*, **372**, 20130084
 France, K., Loyd, R. O. P., Youngblood, A., et al. 2016, *ApJ*, **820**, 89
 Gaia Collaboration, Brown, A. G. A., Vallenari, A., et al. 2016, *A&A*, **595**, A2
 Gaia Collaboration, Brown, A. G. A., Vallenari, A., et al. 2021, *A&A*, **649**, A1
 Gillon, M., Jehin, E., Lederer, S. M., et al. 2016, *Natur*, **533**, 221
 Grenfell, J. L., Stracke, B., von Paris, P., et al. 2007, *P&SS*, **55**, 661
 Grenfell, J. L., Leconte, J., Forget, F., et al. 2020, *SSRv*, **216**, 98
 Guo, X., Crossfield, I. J. M., Dragomir, D., et al. 2020, *AJ*, **159**, 239
 Guo, Z., Gully-Santiago, M., & Herczeg, G. J. 2018, *ApJ*, **868**, 143
 Hawley, S. L., Gizis, J. E., & Reid, I. N. 1996, *AJ*, **112**, 2799
 Hoge, E. R. 1947, *PASP*, **59**, 109
 Hogg, D. W., & Foreman-Mackey, D. 2018, *ApJS*, **236**, 11
 Hu, R., Seager, S., & Bains, W. 2012, *ApJ*, **761**, 166
 Husser, T.-O., Wende-von Berg, S., Dreizler, S., et al. 2013, *A&A*, **553**, A6
 Irwin, J. M., Charbonneau, D., Esquerdo, G. A., et al. 2018, *AJ*, **156**, 140
 Kempton, E. M. R., Lupu, R., Owusu-Asare, A., Slough, P., & Cale, B. 2017, *PASP*, **129**, 044402
 Kipping, D. M. 2010, *MNRAS*, **408**, 1758
 Kipping, D. M. 2013, *MNRAS*, **435**, 2152
 Kite, E. S., & Barnett, M. N. 2020, *PNAS*, **117**, 18264
 Kopparapu, R. K., Ramirez, R., Kasting, J. F., et al. 2013, *ApJ*, **765**, 131
 Kostov, V. B., Schlieder, J. E., Barclay, T., et al. 2019, *AJ*, **158**, 32
 Kreidberg, L. 2015, *PASP*, **127**, 1161
 Kreidberg, L., Bean, J. L., Désert, J.-M., et al. 2014, *Natur*, **505**, 69
 Libby-Roberts, J. E., Berta-Thompson, Z. K., Désert, J.-M., et al. 2020, *AJ*, **159**, 57
 Lightkurve Collaboratio, Cardoso, J. V. d. M., Hedges, C., et al. 2018, Lightkurve: Kepler and TESS time series analysis in Python, Astrophysics Source Code Library, ascl:1812.013
 Lopez, E. D., & Fortney, J. J. 2013, *ApJ*, **776**, 2

- Luger, R., & Barnes, R. 2015, *AsBio*, 15, 119
- Luque, R., Pallé, E., Kossakowski, D., et al. 2019, *A&A*, 628, A39
- Mandal, S., Hegde, M., Samanta, T., et al. 2017, *A&A*, 601, A106
- Ment, K., Dittmann, J. A., Astudillo-Defru, N., et al. 2019, *AJ*, 157, 32
- Ment, K., Irwin, J., Charbonneau, D., et al. 2021, *AJ*, 161, 23
- Morley, C. V., Fortney, J. J., Kempton, E. M.-R., et al. 2013, *ApJ*, 775, 33
- Morris, B. M., Curtis, J. L., Sakari, C., Hawley, S. L., & Agol, E. 2019, *AJ*, 158, 101
- Mugnai, L. V., Modirrousta-Galian, D., Edwards, B., et al. 2021, *AJ*, 161, 284
- Newton, E. R., Irwin, J., Charbonneau, D., et al. 2016, *ApJ*, 821, 93
- Newton, E. R., Mondrik, N., Irwin, J., Winters, J. G., & Charbonneau, D. 2018, *AJ*, 156, 217
- Nicholson, S. B. 1948, *PASP*, 60, 98
- Nutzman, P., & Charbonneau, D. 2008, *PASP*, 120, 317
- Owen, J. E., Shaikhislamov, I. F., Lammer, H., Fossati, L., & Khodachenko, M. L. 2020, *SSRv*, 216, 129
- Owen, J. E., & Wu, Y. 2017, *ApJ*, 847, 29
- Parviainen, H., & Aigrain, S. 2015, *MNRAS*, 453, 3821
- Pont, F., Knutson, H., Gilliland, R. L., Moutou, C., & Charbonneau, D. 2008, *MNRAS*, 385, 109
- Rackham, B. V., Apai, D., & Giampapa, M. S. 2018, *ApJ*, 853, 122
- Rackham, B. V., Apai, D., & Giampapa, M. S. 2019, *AJ*, 157, 96
- Schaefer, L., Wordsworth, R. D., Berta-Thompson, Z., & Sasselov, D. 2016, *ApJ*, 829, 63
- Segura, A., Krellove, K., Kasting, J. F., et al. 2003, *AsBio*, 3, 689
- Sing, D. K., Pont, F., Aigrain, S., et al. 2011, *MNRAS*, 416, 1443
- Southworth, J., Mancini, L., Madhusudhan, N., et al. 2017, *AJ*, 153, 191
- Swain, M. R., Estrela, R., Roudier, G. M., et al. 2021, *AJ*, 161, 213
- Trifonov, T., Caballero, J. A., Morales, J. C., et al. 2021, *Sci*, 371, 1038
- Tsiaras, A., Waldmann, I. P., Rocchetto, M., et al. 2016a, *ApJ*, 832, 202
- Tsiaras, A., Rocchetto, M., Waldmann, I. P., et al. 2016b, *ApJ*, 820, 99
- Vanderspek, R., Huang, C. X., Vanderburg, A., et al. 2019, *ApJL*, 871, L24
- Waalkes, W. C., Berta-Thompson, Z., Bourrier, V., et al. 2019, *AJ*, 158, 50
- Wakeford, H. R., Sing, D. K., Evans, T., Deming, D., & Mandell, A. 2016, *ApJ*, 819, 10
- Wakeford, H. R., Lewis, N. K., Fowler, J., et al. 2019, *AJ*, 157, 11
- Winn, J. N. 2010, in *Exoplanets*, ed. S. Seager (Tucson, AZ: Univ. of Arizona Press), 55
- Winters, J. G., Medina, A. A., Irwin, J. M., et al. 2019, *AJ*, 158, 152
- Zhang, Z., Zhou, Y., Rackham, B. V., & Apai, D. 2018, *AJ*, 156, 178
- Zhou, Y., Apai, D., Lew, B. W. P., & Schneider, G. 2017, *AJ*, 153, 243